

COHERENT VORTICES IN THE ARGENTINE BASIN

by

JUNLIN CHEN

A Thesis Submitted to
The Hong Kong University of Science and Technology
in Partial Fulfillment of the Requirements for
the Degree of Master of Philosophy
in Marine Environmental Science

July 2022, Hong Kong

Authorization

I hereby declare that I am the sole author of the thesis.

I authorize the Hong Kong University of Science and Technology to lend this thesis to other institutions or individuals for the purpose of scholarly research.

I further authorize the Hong Kong University of Science and Technology to reproduce the thesis by photocopying or by other means, in total or in part, at the request of other institutions or individuals for the purpose of scholarly research.

JUNLIN CHEN

COHERENT VORTICES IN THE ARGENTINE BASIN

by

JUNLIN CHEN

This is to certify that I have examined the above M.Phil. thesis
and have found that it is complete and satisfactory in all respects,
and that any and all revisions required by
the thesis examination committee have been made.

PROF. WANG YAN, THESIS SUPERVISOR

PROF. STANLEY LAU, HEAD OF DEPARTMENT

Department of Marine Environmental Science

22 July 2022

ACKNOWLEDGMENTS

My research career has been accompanied by the Covid-19 pandemic. I would never have completed this work without the help of many people.

First of all, I want to express my greatest appreciation for my supervisor, Professor WANG Yan, for his years of hands-on physical training, continuous advice, and kindly support. I have learned the beauty of understanding the ocean from a physical and discrete mathematical way, and known how to develop, organize, and express my ideas in scientific research. He also encourages me in many aspects of research and life. These skills and guidance are crucial for my later career development.

I thank the members of my thesis committee, Professor Julian Mak and Professor Li Jiying for their insightful comments to help me polish this work.

I would like to thank my group members and colleagues in HKUST – Mr. WEI Huaiyu, Ms. CHAI Xia, Mr. DENG Peng, Ms. ZHANG Ying, Mr. CHENG Weichong, Dr. LI Dou, Dr. XIE Chenyue, and Ms. QUAN Mingyu. I spent most of my colorful graduate life with them, learned most of the necessary academic skills from senior students, and got moral support from them.

I also want to thank my supervisor and the Department of Ocean Science (OCES) for providing me with a postgraduate scholarship and offering me such a precious opportunity to explore the mysteries of the world from the perspective of the physical oceanography.

Last but not least, I thank my family members, for my parents' great support in mental and physical health. I wanted to share every moment of happiness and each stage of success with them.

TABLE OF CONTENTS

Title Page	i
Authorization Page	ii
Signature Page	iii
Acknowledgments	iv
Table of Contents	v
List of Figures	viii
List of Tables	x
Abstract	xi
Chapter 1 Introduction	1
1.1 Oceanic eddies	1
1.2 The flow pattern of the Argentine Basin	3
1.3 Traditional vortex detection methods	5
1.4 Lagrangian coherent structures	8
1.5 Dynamic Mechanisms of the Mesoscale Eddy	11
1.6 Main content and Organization of the paper	12

Chapter 2 data and methodology	14
2.1 Research background	14
2.1.1 Data description	14
2.1.2 Introduction to the study area	15
2.2 Traditional Eulerian method and its drawback	17
2.3 Objective Lagrangian eddies detection	18
2.3.1 Computation setup	19
Chapter 3 Comparison of different eddy detection methods	25
3.1 Introduction of Mesoscale Eddy Trajectory Atlas	25
3.2 Statistics results of Eulerian detection method	25
3.3 Comparison of Lagrangian and Eulerian methods	29
3.4 Conclusion	34
Chapter 4 Eddies features analysis	35
4.1 Eddies statistics	35
4.2 Eddies coherence time	46
4.3 Conclusion	51
Chapter 5 Three-dimensional eddies structures	52
5.1 Introduction	52
5.2 3D structure construction algorithms for an eddy	54
5.3 Eddies penetration depth and three-dimensional shape type	54
5.4 Case studies of oceanic eddies	56
5.5 Discussion and Conclusion	61

Chapter 6 Conclusion and prospect	62
6.1 Statistics result of coherent eddies in the Argentine Basin	62
6.2 Three-dimensional structure of coherent eddies	62
6.3 Future work plan	62
References	64

LIST OF FIGURES

1.1	Image of visible eddies and currents photographed by NASA	2
1.2	Isopycnal displacements associated with three types of eddies [1]	3
1.3	Global distribution of the zonal water transport carried by eddies [2]	4
1.4	Closed vorticity contour in the turbulence flow [3]	6
1.5	A schematic summary of the automated eddy identification procedure for the case of an anticyclonic eddy [4]	7
1.6	Lagrangian coherent structures [5]	8
1.7	Observable Coherent Lagrangian patterns(The Great Red Spot) [6]	9
1.8	A mismatch between a repelling LCS and FTLE ridges[7]	10
2.1	Topographic map of the research region	16
2.2	Surface current pattern of the research area	17
2.3	Schematic of a closed shearline (elliptic transport barrier) [8]	22
2.4	Comparison of ordinary material line and coherent material line [9]	23
3.1	Anticyclonic eddies numbers from 1993 to 2019	26
3.2	Cyclonic eddies numbers from 1993 to 2019	27
3.3	Anticyclonic eddies trajectories from 1993-2018	28
3.4	Cyclonic eddies trajectories from 1993-2018	29
3.5	Monthly and annual volume change characteristics of Eulerian eddy	30
3.6	Seasonal and annual variation of Eulerian eddy number and radius	30
3.7	Cyclonic Eulerian eddy lifetime Frequency	31
3.8	Anticyclonic Eulerian eddy lifetime Frequency	32

3.9	Evolution of one elected eddy	33
4.1	Eddy number per month and per month	36
4.2	Eddy radius frequency distribution histogram	37
4.3	Relationship of vortex radius with latitude	38
4.4	Relationship of vortex stretching ratio with latitude	39
4.5	Relationship of eddy velocity (km) with latitude	40
4.6	Relationship of zonal and meridional velocity with latitude	41
4.7	Eddy polarity distribution map	42
4.8	Monthly and annual patterns of eddy number of different polarities	43
4.9	Monthly and annual patterns of eddy radius of different polarities	44
4.10	Eddy travel direction map	45
4.11	Some vortex examples (orange for cyclonic eddy and blue for anti-cyclonic eddy)	47
4.12	Eddy properties and their relationship with coherence time	48
4.13	Eddy type proportion map	49
4.14	Trajectories map of three 120-day vortices	50
5.1	Histogram distribution map of vortex depth	55
5.2	Three examples of bowl-shaped eddies	57
5.3	Three examples of lens-shaped eddies	57
5.4	Three examples of cone-shaped eddies	58
5.5	Vertical structure of a cyclonic eddy	59
5.6	Vertical structure of an anticyclonic eddy	60

LIST OF TABLES

1.1 Water mass vertical distribution	5
--------------------------------------	---

COHERENT VORTICES IN THE ARGENTINE BASIN

by

JUNLIN CHEN

Department of Marine Environmental Science

The Hong Kong University of Science and Technology

ABSTRACT

Oceanic coherent vortices are swirling bodies of water that play a crucial role in modulating the ocean material transport and circulation. This graduation thesis focuses on the characteristics of coherent vortices in the Argentine basin (AB), a key region for the Southern Ocean mode water formation. An objective Lagrangian method (LAVD) was adopted to extract the coherent vortices in the AB from 1993 to 2019 via satellite altimetry data. By comparing with results obtained by the Eulerian method, we verified the accuracy and robustness of the LAVD method. A sum of 6212 coherent vortices were detected, with their geographical distribution, polarity, and migration patterns investigated. At last, we applied the same algorithm to SOSE dataset and extracted the three-dimensional structure of the eddies from 2013 to 2018.

CHAPTER 1

INTRODUCTION

1.1 Oceanic eddies

Oceanic mesoscale eddies refer to swirling bodies of water that could resist stretching and have semi-diameter ranging from 20 km to 100 km [10, 11]. They carry high concentrations of carbon, chlorophyll, and nutrient, isolate themselves from the surrounding water and have a life circle of several months. Thus, they play a significant role in marine material transport of heat, mass such as nutritive salts, and momentum and have a great impact on global ocean circulation and long-range climate change [1, 12, 5, 13]. A comprehensive and systematic investigation of vortex characteristics (including statistical characteristics and three-dimensional structures, etc) contributes to the understanding of the oceanic dynamical process.

Figure 1.1 is a snapshot of Perpetual Ocean which shows ocean surface currents produced by model output (ECCO2). We could observe a lot of spiral-shaped eddies (marked in red circles) which trap certain amount of water inside in the figure.

Figure 1.2 shows how eddies deflect the density interfaces, deepen or shallow pycnocline (two density surfaces are seasonal thermocline ρ_1 and main thermocline ρ_2), and generate associated upwelling or downwelling. Thus nutrients can be brought up to the surface and down to the interior during the evolution of the eddies, which means that eddies directly affect the biogeochemistry process.

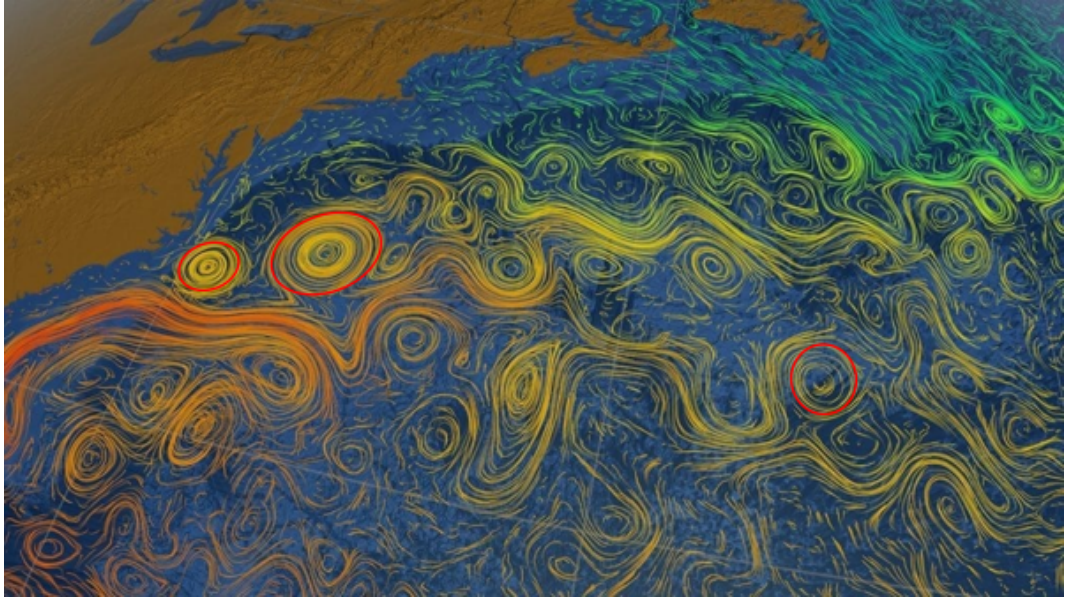


Figure 1.1: Image of visible eddies and currents photographed by NASA

Previous studies have shown that eddy-induced fluid volume zonal transport can reach up to $30 \sim 40$ Sv, which is as much as the large-scale wind-driven or thermohaline circulation [2]. In figure 1.3, part A of the figure shows us the result of eddy-induced zonal transport per latitude based on the mean eddy propagation speed and trapped fluid volume while part B of the figure illustrates the total meridionally integrated zonal transport induced by eddies (blue curve here represents the westward transport and the red curve represents the eastward transport). The studies serve as the evidence of mesoscale eddies' role in the heat, energy, and flux transport.

The tremendous advances in ocean observational methods, especially measurements of ocean surface sea level anomaly, and altimetry-derived velocity fields enable the long-term detection of mesoscale vortices. An increasingly high-resolution and submesoscale-permitting ocean circulation model provides a panoramic view of the three-dimensional ocean flow.

Thus, detection and tracking of coherent ocean eddies have increasingly become a research hot spot.

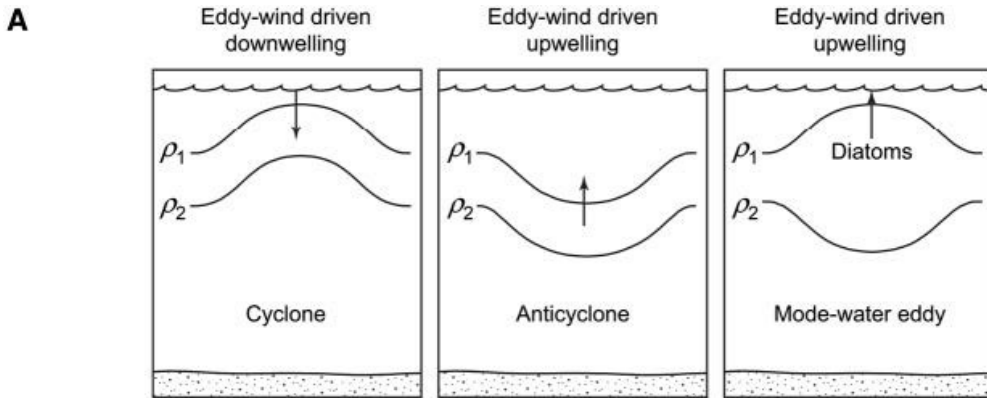


Figure 1.2: Isopycnal displacements associated with three types of eddies [1]

1.2 The flow pattern of the Argentine Basin

The Argentine Basin region, characterized by its basin structure, exhibits several different types of surface and subsurface currents and unique temperature and salt structures.

The Brazil-Malvinas region is characterized by the confluence of southward transport Brazil Current (BC) and northward transport Malvinas Current (MC). Previous studies shows that BC transports about 25 Sv ($1\text{Sv} = 10^6 \text{m}^3 \text{s}^{-1}$) warm ($\theta > 10^\circ\text{C}$) and salt ($S > 35$) water and MC transports about 30-40 Sv cold ($\theta < 7^\circ\text{C}$) and fresh ($S < 34.3$) water into the Brazil-Malvinas region [14]. The mixture of these two distinct water bodies would generate strong salinity and thermal gradient and cause mesoscale instabilities, which is expected to result in large amounts of oceanic eddies [15].

The great variability of the dynamic topography also gives rise to the anisotropic feature in the study region. For example, in the center of the Argentine Basin, Zapiola Anticyclone (ZA) is trapped by a seamount called the Zapiola Rise and the flow greatly inhibits the lateral transport of water, traps water inside, and increases vertical movement such as downwelling transport into the bottom Ekman layer [16, 17, 18].

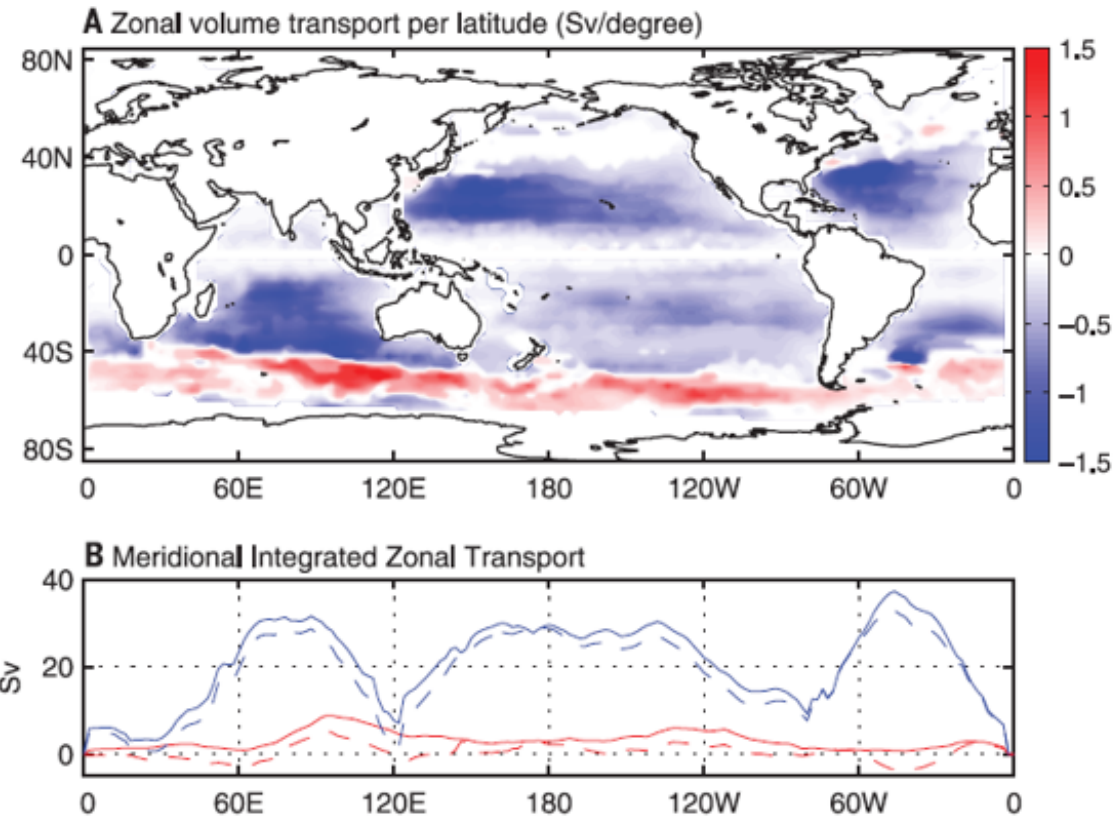


Figure 1.3: Global distribution of the zonal water transport carried by eddies [2]

What is more, the Argentine Basin is regarded as the main channel connecting the Southern Ocean and the Atlantic Ocean, and the properties of water masses inside the Argentine Basin are quite complicated. For example, looking down from the surface, the salinity of the surface-layer water is quite low, and the salinity becomes higher when it mixes with the North Atlantic Deep Water at about 1500-3500 m depth and it becomes a little fresher when it goes down into Antarctic Bottom Water [19]. The vertical distribution of water bodies is listed in the table 1.1 [20]:

Due to the dynamic changes of the current and strong mixing in the study region, lots of energetic mesoscale eddies having great impact on heat and salt budgets were observed.

Table 1.1: Water mass vertical distribution

Water mass	Depth	Density ($\text{kg} \cdot \text{m}^{-3}$)
South Atlantic Central Water	100 - 300 m	$\sigma \leq 26.5$
Sub Antarctic Mode Water	300 - 600 m	$26.5 < \sigma < 27.1$
Antarctic Intermediate Water	600 - 1000m	$27.1 < \sigma < 27.4$
North Atlantic Deep Water	1000 - 400 m	$27.4 < \sigma < 45.90$
Antarctic Bottom Water	towards the sea floor	$\sigma \geq 45.90$

1.3 Traditional vortex detection methods

Traditional automated Eulerian eddy detection methods can be divided into three types [10]: physical parameter-based algorithm using the value exceeding a threshold to identify eddies, flow geometry-based methods focusing on the morphology of the instantaneous streamlines to extract vortices, and hybrid approach taking both the physical parameters and geometric features into consideration.

McWilliams developed the earliest automatic eddy detection algorithm for decaying two-dimensional turbulence. The detection procedure is as follows: at first, we pick a two-dimensional extreme (maximum or minimum) in vorticity (ξ) as their center, and then identify the boundary as the points set with the criterion of $\frac{\xi}{\xi_c} \geq \Delta$ (ξ_c is the vorticity of the vortex center and Δ is the limiting value and 0.2 might be a satisfactory value) as shown in figure 1.4. Besides setting vorticity as the physical parameter, geometric characteristics are also taken into consideration: several shape quantities are raised to ensure that the boundary and interior of the candidate eddy should not depart excessively from asymmetry [3]. This method belongs to the hybrid one.

Among the overall methods, the most popular Eulerian methods are the SSHA method([21]),

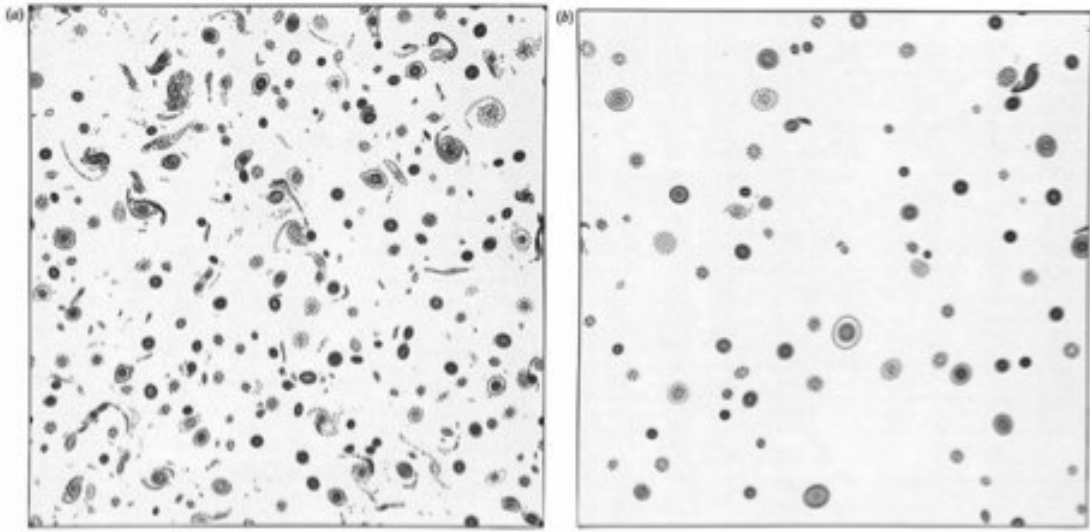


Figure 1.4: Closed vorticity contour in the turbulence flow [3]

and Okubo-Weiss method. SSHA method considers sea level anomalies exceeding a threshold as an eddy and consider the local minimum (maximum) of SSH for cyclonic (anticyclonic) eddies [4]. However, this method lacks the ability to distinguish wave-like structures with eddies. Okubo-Weiss method detects eddies based on Okubo-Weiss parameter, W , which defines eddies by stretch (s_s), shear (s_n), and relative vorticity (ω) in the flow field and the rotation-dominated case ($W < 0$) is considered as vortex [22, 23]. $W = -2 \times 10^{-12} \text{ s}^{-2}$ contours is used to extract eddies in global study.

$$W = s_s^2 + s_n^2 - \omega^2 \quad (1.1)$$

$$s_n = \frac{\partial u'}{\partial x} - \frac{\partial v'}{\partial y}, \quad s_s = \frac{\partial v'}{\partial x} + \frac{\partial u'}{\partial y}, \quad w = \frac{\partial v'}{\partial x} - \frac{\partial u'}{\partial y} \quad (1.2)$$

Via geostrophic balance, u' and v' may be calculated by the gradient of sea level anomaly.

$$u' = -\frac{g}{f} \frac{\partial(SLA)}{\partial y}, \quad v' = \frac{g}{f} \frac{\partial(SLA)}{\partial x} \quad (1.3)$$

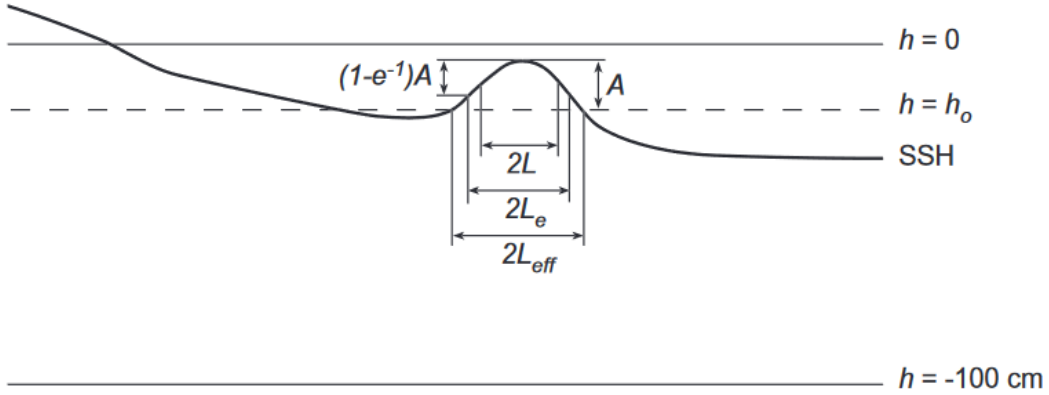


Figure 1.5: A schematic summary of the automated eddy identification procedure for the case of an anticyclonic eddy [4]

However, above Eulerian diagnostics are unreliable since they are not objective and depend on thresholds. Being not objective means that the results would perform differently when viewed from different reference frames. In other words, the existence of the eddy is questionable and the transport of material carried by eddy is not guaranteed to be coherent. Depending on thresholds signifies that the results of the detection would vary a lot and the boundary would disagree with each other when choosing different thresholds. In the following chapter 1.4, we would turn to a new concept of Lagrangian coherent structures and how it is related to the detection of oceanic eddies.

1.4 Lagrangian coherent structures

Recently, breakthroughs at the crossroads of nonlinear dynamical systems theory and fluid dynamics has promoted the application of detecting the vortices in a variety of fields. As shown in figure 1.6, in the field of dynamical systems, Lagrangian coherent structures (LCSs) refer to material lines or surfaces that attract, repel, or shear the most, which uncover the geometric property of the flow field (repelling LCSs tends to induce local stretching, thinning, and folding happen along attracting LCSs boundary, and shear LCSs describe swirling pattern [24]), and thus play a significant role in the study of chaotic advection and material mixing [6, 25, 26]. Material coherence is observable everywhere in nature: Great Red Spot photographed by Voyager 1 in 1979 and processed by Bjorn Jonsson as shown in figure 1.7. Because LCSs could influence the particles around them more than others, which means that this structure is not transient, thus a structure is considered coherent if it lasts a long time in the flow of the observed fluid [5]. In other words, LCSs could not be crossed by material and act as transport barrier, thus providing solid framework to detect coherent eddies.

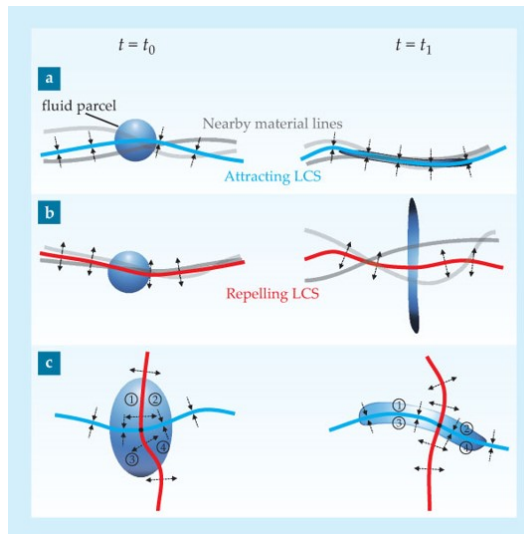


Figure 1.6: Lagrangian coherent structures [5]



Figure 1.7: Observable Coherent Lagrangian patterns(The Great Red Spot) [6]

Instead of observing fluid properties from a fixed frame in chapter 1.3 (Eulerian representation), Lagrangian dynamics focus on the motion of specific parcels of fluid and follow them through space [27]. Assessment of flow patterns from a single tracer is impractical because of the sensitivity of fluid-particle trajectories to initial conditions; however, LCSs provide a solid framework of material surfaces and thus enable the comparison of models and other observational data[6].

However, LCSs in ocean turbulence are not well-defined and interpreted as material loops showing little deformation, no filamentation, and consistent area during the so-called LCSs life cycle, which would last for several weeks to several months. LCSs are believed to be bounded by uniformly stretching fluid line and maintain the arc length during the transport period. Such coherent structures will confine mixing and material exchange between the water body trapped inside and ambient ocean turbulent flow and thus quantify important aspects of material transport[6].

Recently, several Lagrangian methods have been developed to accurately predict the material transport barrier in geophysical flows: ridges of finite-time Lyapunov exponent (FTLE) [28, 29], and finite-size Lyapunov exponent (FSLE) [30, 31, 32]. Haller proposed that the ridge of FTLE would be an indicator of hyperbolic LCSs (repelling in forward time and attracting in backward time) [33]. However, it still remains uncertain about the relationship between FTLE or FSLE with LCS and some counterexamples have doubted the robustness of the detection method [7, 34]. As shown in figure 1.8, there is an observable repelling LCS along y-axis in the nonlinear strain flow while FTLE ridges are not detected in this case (constant forward FTLE field) [7]. In classic dynamical systems, this recurrent structure is called the saddle fixed point.

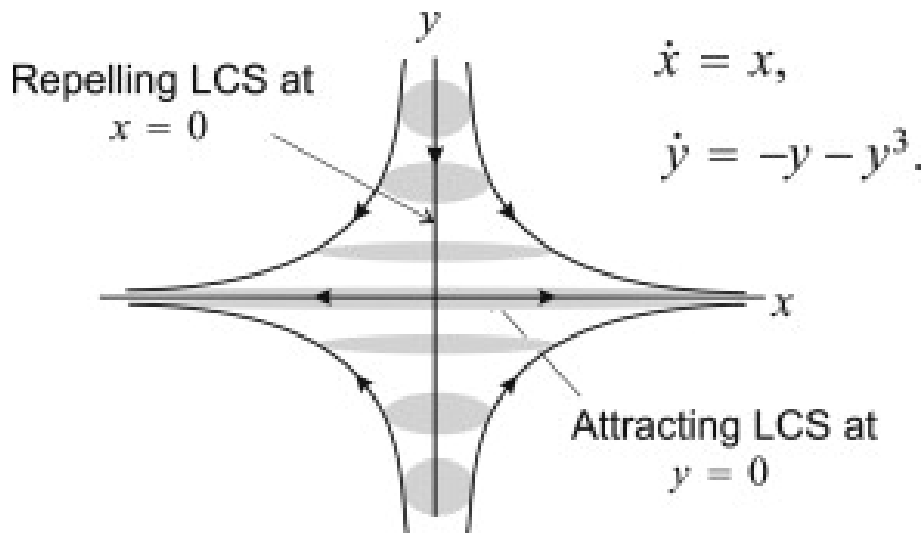


Figure 1.8: A mismatch between a repelling LCS and FTLE ridges[7]

In order to reduce the false positive and false negative results in coherent structure detection, a redefinition with rigorous mathematics is needed.

1.5 Dynamic Mechanisms of the Mesoscale Eddy

According to previous studies, the properties and formation of eddies were strongly related to the evolution of baroclinic instability caused by vertical velocity shear between different layers [35, 36].

Complex flow-vortex interactions with strong currents near the western boundary could also explain the complicated LCSs in the study region.

Other dynamical factors such as mixed layer instabilities, frontal dynamics, buoyancy anomalies produced by sea ice leads and so on could also affect the formation and evolution process of LCSs [37, 38].

How relative wind stress acts on eddies is controversial: some researchers think that it would depress the development of eddies and performs as the “killer” of eddies’ kinetic energy [39, 40]; however, an updated study have demonstrated that eddies can response and adjust to the wind and the work done by relative wind stress on eddies could turn from negative to positive after the ”inflection point” [41].

1.6 Main content and Organization of the paper

As mentioned above, studies of mesoscale eddies are now the research hotspots due to the importance of eddies' role. However, studies of basic statistical characteristics of the vortex, the three-dimensional structure of the vortex, and its influence on the vertical distribution of temperature and salt are not very clear in Argentine Basin. We want to understand the following questions: (1) How deep do the ocean eddies extend? (2) What is the shape of ocean eddies? (3) How many eddies could be detected and what are the characteristic features of the ocean eddies? (4) Given the same domain and same velocity field generated by the numerical model, how different it will be when different methods are adopted?

The thesis includes six chapters, and it starts with a brief introduction to the ocean eddies detection methods and flows pattern of the Argentine Basin. Chapter Two mainly discuss the detailed setup process of the eddy's detection.

Chapters Three to Five contain the main body of this thesis and cover the eddies properties, three-dimensional eddies profile, and comparison of several different methods in the eddy detection process. The last chapter draws a general conclusion from the above content and outlines several future research directions.

To be specific, Chapter Two gives mathematical images and formulas of nonlinear dynamics and geodesic theory and its application to geostrophic flow. Since the content is not intuitive enough, someone who is not familiar with the notion may skip this chapter and backtrack the chapter as a reference when needed. What is more, we also discuss the drawback of traditional Eulerian method, which is the base of Chapter Three.

Chapter Three focuses on the comparison of Eulerian methods and Lagrangian methods and

verifies the robustness of LAVD method. The similarities and differences between these results are discussed here.

Chapter Four concerns the statistical quantity of the ocean eddies such as their radius, polarity and population. We show that most eddies maintain their coherent feature during the transport, which lays a solid foundation for accurately quantifying the eddies-induced transport in Argentine Basin.

In Chapter Five, we explore the three-dimensional structure of the vortex and discuss the vertical extension of eddies from the surface to subsurface.

Chapter Six makes a conclusion of the work and provides an outlook and forecast of possible future work.

CHAPTER 2

DATA AND METHODOLOGY

In this chapter, we first introduce the data used in the study, and the flow pattern of the research area. Then, we give a brief introduction to the available velocity-based estimates of oceanic eddies, summarize their characteristics and point out their limits and deficiency such as the inability of capturing long-term transport mechanisms and inconsistency in different reference frames. At last, we focus on the computation setup workflow of the objective Lagrangian eddy detection methods.

2.1 Research background

2.1.1 Data description

In the study, we combine the remote sensing satellite altimetry data and oceanic model data.

Satellite altimetry gives a new perspective on sea surface topography anomaly observation by providing full coverage of the ocean surface measurements. By analyzing sea level anomaly (SLA) from the AVISO product (<https://www.aviso.altimetry.fr/en/home.html>) between January 1993 to December 2019, we can learn the long-term climatology characteristics of the oceanic eddies. AVISO SLA data combines a series of satellites data such as Ocean Topography Experiment (TOPEX) / Poseidon and European Remote Sensing Satellite (ERS) altimeter data, and then all the weekly product was interpolated to $\frac{1}{4}^\circ \times \frac{1}{4}^\circ$ spatial resolution grid points based

on the Mercator projection method, which provides oceanographer with solid and continuous upper ocean mesoscale information [11, 42, 43, 44].

Ocean model data provides us with three-dimensional oceanic flow information, which contributes to the three-dimensional construction of ocean vortex structures and helps us understand the volume transport. In the study, we apply the same methodology to the Southern Ocean State Estimate (SOSE) dataset at each depth level and the time span is from 2013 to 2018, which covers part of the time period of the AVISO altimetry data [45, 46]. Thus, we could construct the three dimensional structures and calculate mass transport carried by eddies [47].

The flow velocity is established on the basis of geostrophic balance theory which assumes that the sea pressure gradient force induced by sea surface slope and Coriolis force are approximately equal:

$$\mathbf{v}(\mathbf{x}, t) = \left[-\frac{g}{f} \frac{\partial \eta(\mathbf{x}, t)}{\partial y}, \frac{g}{f} \frac{\partial \eta(\mathbf{x}, t)}{\partial x} \right] \quad (2.1)$$

$\mathbf{x} = (x, y)$ denotes the zonal and meridional velocity; $\eta(\mathbf{x}, t)$ denotes sea surface height (SSH); f is the vertical component of Coriolis force; and g is the acceleration of gravity [8].

The variation of SSH is calculated from the gap between altimeter SSH anomaly data and the mean dynamic topography. The background η is assumed to be steady and the perturbation part of SSH is transient.

2.1.2 Introduction to the study area

The latitude range of the research area is between 30S and 60S and the longitude ranges from 70W to 30W as shown in figure 2.1. The main study region could be separated into four zones:

Argentine Basin (AB) covering most of the northeast part of the study region; Southern Ocean (SO) region; connecting waters between AB and SO. The Argentine Basin is of flattened-circular shape and bounded by Patagonian Shelf to the west and Rio Grande Rise to the north [48]. We could learn from the map that the central part of the basin is deeper than 4,000 meters and it can reach 600 meters at the southwestern part. South Georgia and the South Sandwich Islands and Falkland Islands lie in the east and west of the study area.

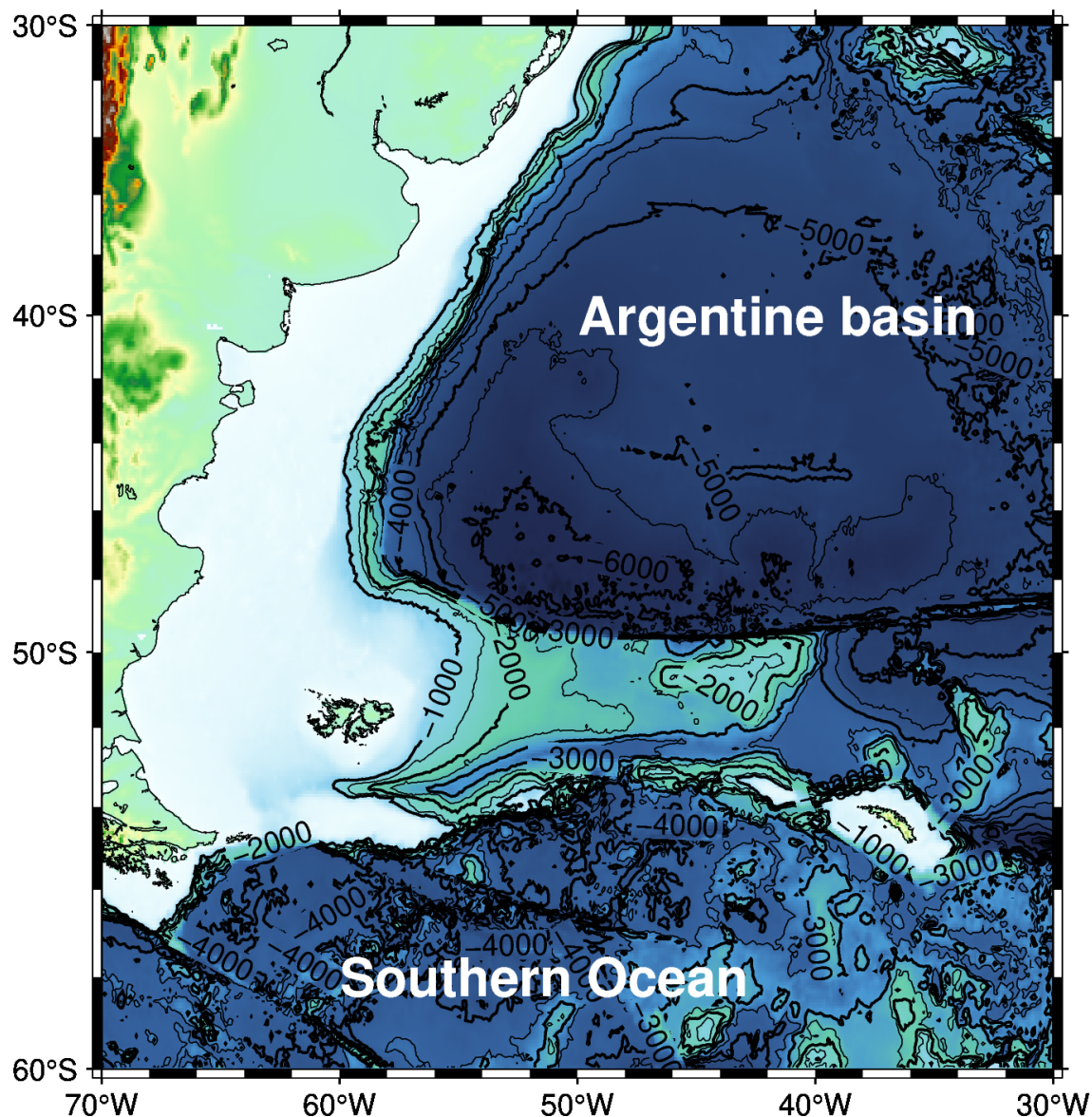


Figure 2.1: Topographic map of the research region

The surface flow pattern of the research region is shown in figure 2.2 and has already been described in chapter 1.2 to show the importance of the study. Southward transport Brazil Current (BC) mix with northward transport Malvinas Current (MC) and form fluctuating Brazil/Malvinas Confluence (BMC) at about 40°S due to wind stress and baroclinic instabilities [14, 48]. An anticyclonic gyre called Zapiola Anticyclone (ZA) around the hill transports considerably large volume of water of about 200 Sv [49].

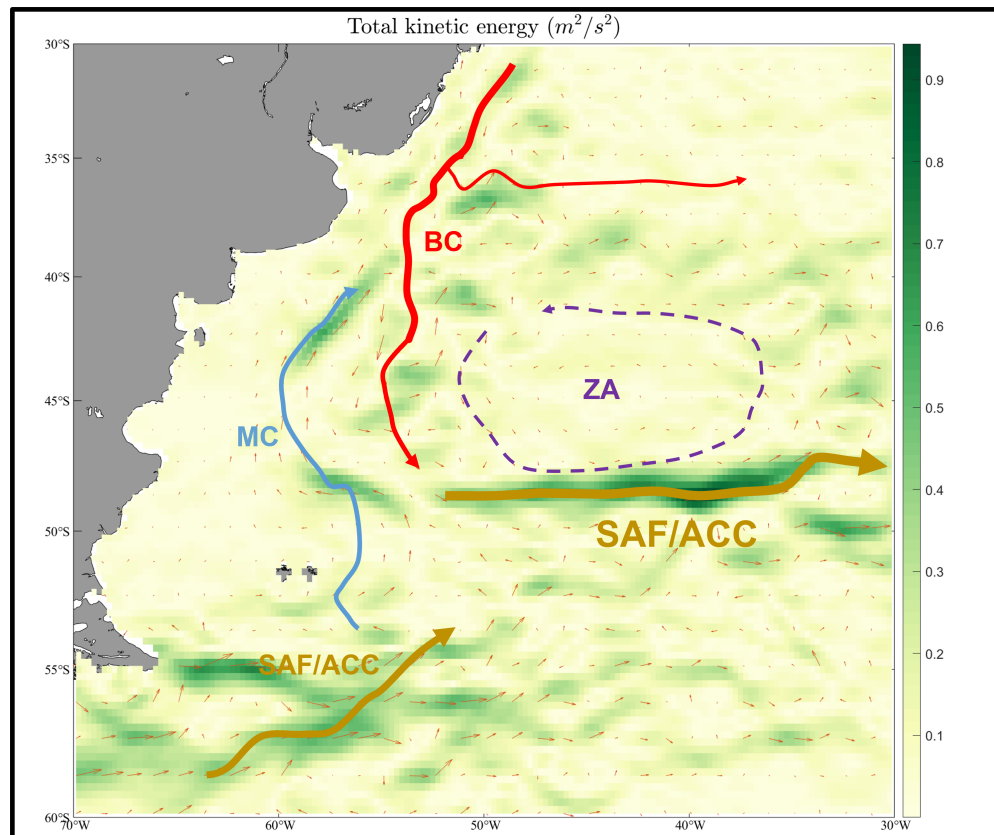


Figure 2.2: Surface current pattern of the research area

2.2 Traditional Eulerian method and its drawback

Since oceanic eddies are regarded as swirling bodies of water that trap a certain number of tracers inside, oceanic eddies are widely acknowledged to be Lagrangian (material).

There are two analytical frameworks for fluid mechanics study: one is the Eulerian method to describe the dynamics properties in a fixed space and the other is the Lagrangian method to describe the fluid properties from the point of view of particle motion [50].

Traditional eddy detection methods are Eulerian methods based on the instantaneous velocity field, which are not robust and may produce spurious results. For example, one of the Eulerian criteria is to seek a closed streamline in unsteady fluid flows; however, this topological feature is not invariant under Galilean transformations, and thus closed streamline may behave differently when choosing different Galilean transformation schemes [50].

As well as the above problems, Eulerian methods depend on the chosen thresholds value, thus the detection result could vary a lot when choosing different thresholds, generating noisy results and making the quantification of eddy transport unreasonable.

2.3 Objective Lagrangian eddies detection

In the last section, we discussed some Eulerian eddy-detection methods which are suitable for analysis of snapshot properties but not for distinguishing long-living structures from the incoherent unsteady flow.

Thus, more attention has been paid to the Lagrangian point of view and characterizes flow patterns in the path line.

The theory for extracting the material boundaries in steady or near-steady flow has been put forward for more than two decades; however, identifying material boundaries in unsteady flow has been a question for long time. Recently, Haller and Beron-Vera developed a new approach to describe transport barrier as the least stretching material line and the closed shearline of γ_{t_0} .

The elliptic transport barrier is computed in the period of $[t_0, t + T]$, acting as the generalized KAM curve and conserving both its arclength and enclosed area until $t_0 + T$ [51]. Thus, the elliptic transport barrier is the desired organization of the eddy candidate region.

The above theory seeks those frame-independent maximal shear as transport barriers and the shear barriers with a bunch of closed curves are called elliptic barriers [52]. The outermost elliptic barrier serves as the eddy boundary and enclosed the maximum area of coherent water mass over the domain[52].

2.3.1 Computation setup

We begin a two-dimensional velocity field $\mathbf{v}(\mathbf{x}, t)$, with \mathbf{x} representing the position in the flow field and fix the time span ($[t_0, t_0 + T]$) for tracking the coherent eddies.

$$\dot{\mathbf{x}}(t) = \mathbf{u}(\mathbf{x}(t), t) \quad (2.2)$$

For two-dimensional, divergence-free flows, we could introduce the stream function $\Psi(x, y)$ and rewrite the velocity in the form of gradient of the stream function. This conversion links the Hamiltonian mechanics and 2-D unsteady flow and makes the detection of invariant manifolds under the flow possible [25].

$$u = \frac{dx}{dt} = \frac{\partial \Psi}{\partial y}, \quad v = \frac{dy}{dt} = -\frac{\partial \Psi}{\partial x} \quad (2.3)$$

We then introduce the concept of flow map $F_{t_0}^{t_0+T}$. This map describes the Lagrangian trajectory of the particle released at initial position x_0 and how it evolves with time.

$$F_{t_0}^{t_0+T} : \mathbf{x}_0 \mapsto \mathbf{x}(t_0 + T; \mathbf{x}_0, t_0) \quad (2.4)$$

In continuum fluid mechanics, we can describe the strain by introducing deformation gradient, and the following equation 2.5 shows how to calculate deformation gradient in 2-dimensional flow fields.

$$\nabla F_{t_0}^t(\mathbf{x}_0) \approx \begin{pmatrix} \frac{x^1(t; t_0, x_0 + \delta_1) - x^1(t; t_0, x_0 - \delta_1)}{|2\delta_1|} & \frac{x^1(t; t_0, x_0 + \delta_2) - x^1(t; t_0, x_0 - \delta_2)}{|2\delta_2|} \\ \frac{x^2(t; t_0, x_0 + \delta_1) - x^2(t; t_0, x_0 - \delta_1)}{|2\delta_1|} & \frac{x^2(t; t_0, x_0 + \delta_2) - x^2(t; t_0, x_0 - \delta_2)}{|2\delta_2|} \end{pmatrix} \quad (2.5)$$

In the above equation, δ_i is a small vector pointing in the x^i coordinate direction.

The right Cauchy–Green strain tensor $\mathbf{C}_{t_0}^{t_0+T}(\mathbf{x}_0)$ is then definded as

$$\mathbf{C}_{t_0}^{t_0+T}(\mathbf{x}_0) = (\nabla \mathbf{F}_{t_0}^{t_0+T}(\mathbf{x}_0))^T \nabla \mathbf{F}_{t_0}^{t_0+T}(\mathbf{x}_0) \quad (2.6)$$

This symmetric tensor is positive definite, thus we could get two real positive eigenvalues λ_i and orthogonal real eigenvectors ξ_i :

$$C\xi_i = \lambda_i \xi_i, \quad |\xi_i| = 1, \quad i = 1, 2; \quad 0 < \lambda_1 \leq \lambda_2, \quad \xi_i \perp \xi_j, \quad i \neq j \quad (2.7)$$

If the flow is incompressible, these two eigenvalues also satisfy the following relations:

$$\det C = \prod_i \lambda_i \equiv 1, \quad 0 < \lambda_1 < 1 < \lambda_2 \quad (2.8)$$

After setting up the invariant dynamical system, we now turn to scalar quantities.

The first technique is by using the Lyapunov exponent, which originates from dynamical system and measures how much close particles spread in the chaotic flow field. This method identifies LCSs as ridges in the Finite time Lyapunov exponent (FTLE) field and thus small or no material flux cross LCSs [28, 33, 53, 29]. This method is widely used in ideal flow experiment.

The Finite time Lyapunov exponent σ is calculated as:

$$\sigma \left(\mathbf{F}_{t_0}^{t_0+T} (\mathbf{x}_0) ; \mathbf{x}_0 \right) = \frac{1}{|T|} \log \sqrt{\lambda_{\max} \mathbf{C}(\mathbf{x}_0)} \quad (2.9)$$

The second method is more rigorous mathematically and identifies the least stretching or de-forming material surface (in 3-D flow) or material line (2-d flow) through a variational theory[54, 7, 51]. This method is more widely used in geophysical flows and recent studies of life cycle of a coherent Agulhas ring and detection of Agulhas Leakage have demonstrated its robustness[52, 55, 8]. First, we assume an initial materine line to be $\mathcal{M}(t_0)$ and then it is advected to be $\mathcal{M}(t_0 + T)$ according to equation 2.10.

$$\mathcal{M}(t_0 + T) := F_{t_0}^{t_0+T} (\mathcal{M}(t_0)) \quad (2.10)$$

To express this coherence principle mathematically, we select a parametrization $r(s)$ with $s \in [0, \sigma]$ for the closed curve γ at time t_0 , and denote the length of a tangent vector $r'(s)$ by $l_{t_0}(s)$. We also let $l_{t_0+T}(s)$ denote the length of the corresponding tangent vector $(d/ds)F_{t_0}^{t_0+T}(r(s))$ along the advected curve $F_{t_0}^{t_0+T}(\gamma)$. These two tangent lengths can be calculated as

$$l_{t_0}(s) = \sqrt{\langle r'(s), r'(s) \rangle}, \quad l_t(s) = \sqrt{\langle r'(s), C_{t_0}^t(r(s))r'(s) \rangle} \quad (2.11)$$

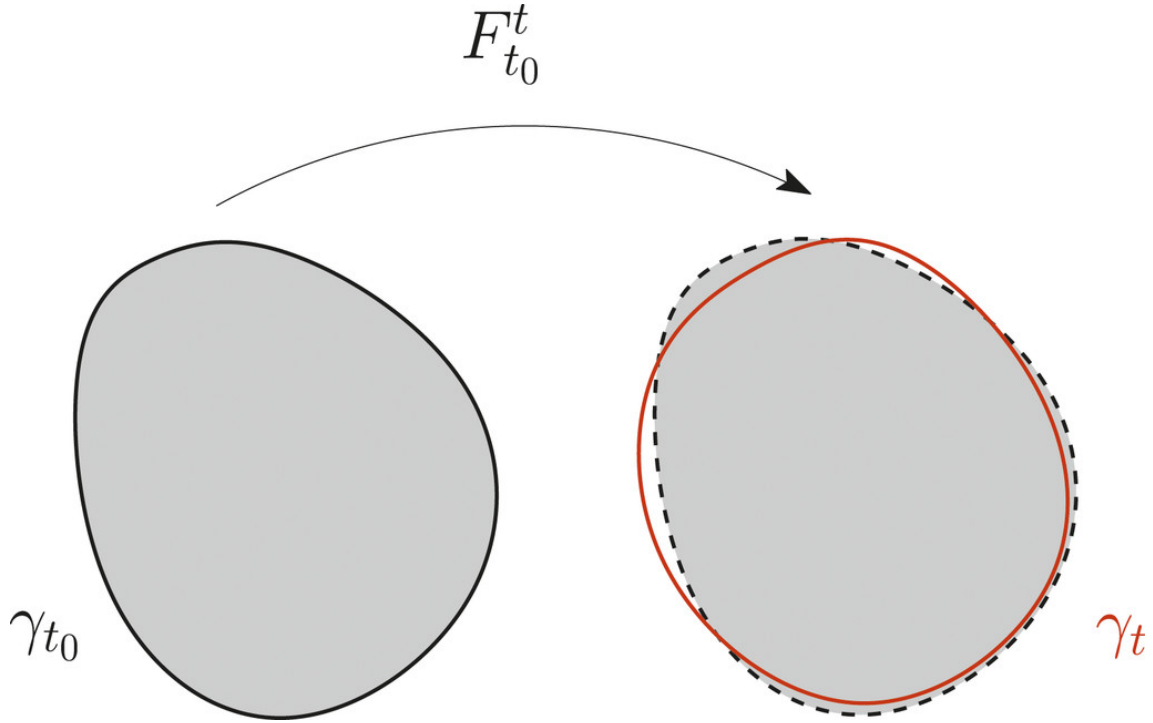


Figure 2.3: Schematic of a closed shearline (elliptic transport barrier) [8]

where $\langle \cdot, \cdot \rangle$ denotes the Euclidean inner product [56]. The averaged tangential strain along γ is then given by

$$Q(\gamma) = \frac{1}{\sigma} \int_0^\sigma \frac{l_{t_0+T}(s)}{l_{t_0}(s)} ds \quad (2.12)$$

As argued above, if an observable coherent material belt exists around γ , then on ε -close material loops we must have $Q(\gamma + \varepsilon h) = Q(\gamma) + O(\varepsilon^2)$, where $\varepsilon h(s)$ denotes small, periodic perturbations to γ . This is only possible if the first variation of Q vanishes on γ :

$$\delta Q(\gamma) = 0 \quad (2.13)$$

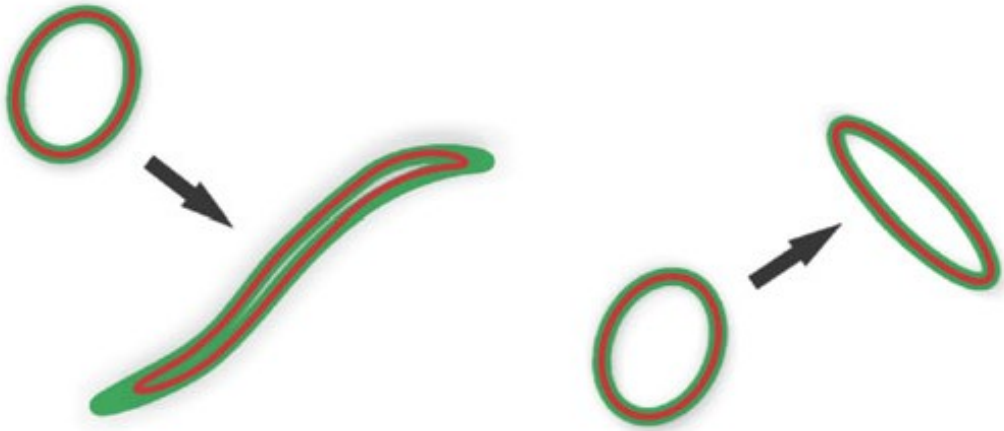


Figure 2.4: Comparison of ordinary material line and coherent material line [9]

The third method for detecting the oceanic eddies is the Lagrangian Averaged Vorticity Deviation (LAVD) method, which is more intuitive and takes the time-integrated deviation of vorticity from background vorticity into consideration [57, 58]. Using this method, vortex center is regarded as the maximum value of $|LAVD|$ and the vortex boundaries are the outermost convex curves around the center. We define coherence over a finite time interval $[t_0, t_0 + T]$, which means that water column remain inside vortex during the period.

$$LAVD_{t_0}^{t_0+T}(x_0) = \int_{t_0}^{t_0+T} |\omega - \bar{\omega}| ds \quad (2.14)$$

In the study, we apply LAVD eddy detection algorithm to altimetry-derived ocean currents starting on the first day of every month from 1993-2019, and the coherence time spans is 30 days. In the next step, we also change the time period from 30 days to 60 days, 90 days, and even 120 days and apply the methods to the model simulation product at each depth. Tracking

coherent eddies in a 27-year period contributes to the understanding of the role of oceanic eddies in the transport process, especially the move of diffusive material and climatology trend of eddies change. The coherence time span varies to test the maximum material coherence of the eddies.

Thus, the workflow for us to apply the eddy detection algorithm to extract oceanic eddies from the flow field is as follows:

- 1) Set up a two-dimensional velocity field to advect the particle.
- 2) Introduce the definition of flow map to show how particles move in the coherent time interval Δt .
- 3) Calculate the deformation gradient and get the Cauchy-Green Strain Tensor.
- 4) Finally, we compute the LCSs from the LAVD field.

CHAPTER 3

COMPARISON OF DIFFERENT EDDY DETECTION METHODS

In this chapter, we evaluate the robustness of the Lagrangian method by comparing the eddy detecting results between SSHA Eulerian method (as illustrated in figure 1.5) and the LAVD method.

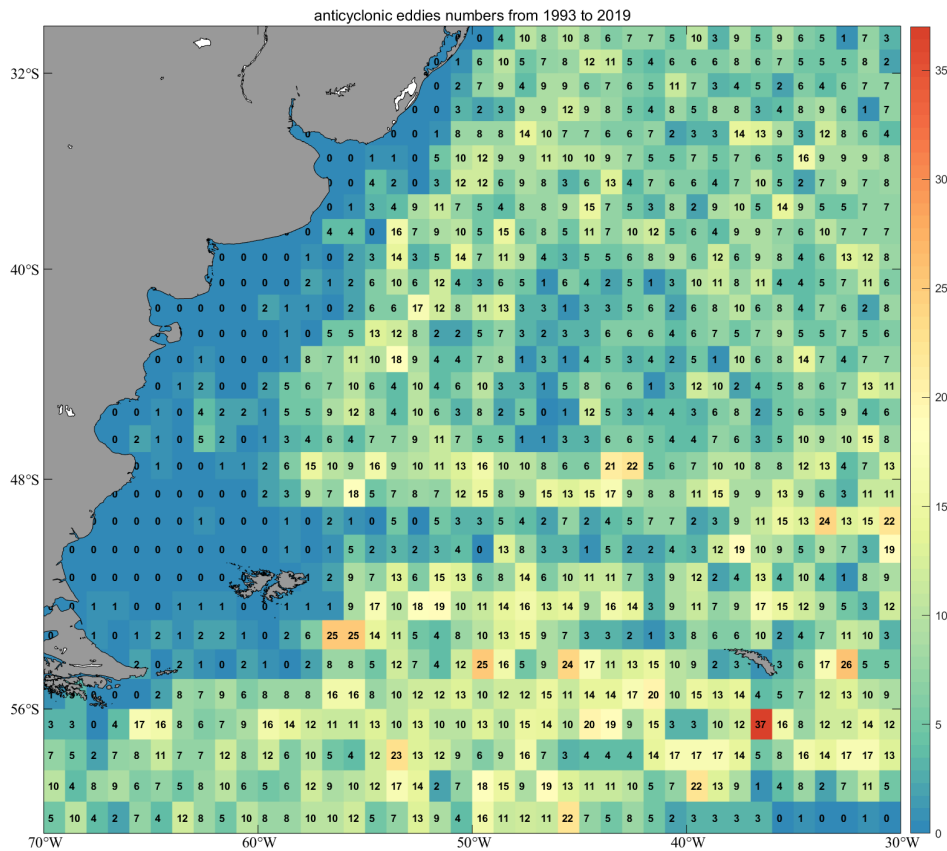
3.1 Introduction of Mesoscale Eddy Trajectory Atlas

We download Eulerian eddies trajectories data from AVISO+, which detected eddies from Sea Level Anomaly field of merged altimetry datasets using SSHA method as described in chapter 1.3 and told us information of type, speed, and radius of Eulerian eddies globally [4]. This dataset contains eddies with a life cycle of more than 4 weeks. The time frame of the dataset is from 1993 to the present. In this chapter, all the eddies in the spatial range 70°W to 30°W , 60°S to 30°S are used for the statistical analysis of Eulerian eddies. The time range of the vortex dataset selected for the study is from January 1993 to December 2019.

3.2 Statistics results of Eulerian detection method

The statistics Eulerian detection results are shown below in figure 3.1 and figure 3.2 (we separate the research region into $1^{\circ} \times 1^{\circ}$ sub-domain and sum up the eddies appearing respectively in

each sub-domain). From 1993 to 2019, 13683 eddies were generated in the whole region, 6686 of them are anti-cyclonic eddies and 6997 are cyclonic ones. Among all the eddies, along the coast of South America, only a few eddies were detected, which is consistent with Lagrangian methods. In the northern part and the southwest part of the Argentine Basin, we observe vast numbers of eddies. In the center part of the Argentine Basin, only a few eddies were detected. Many vortices have been observed in the Southern Ocean region or in the connecting water region between Argentine Basin and the Southern Ocean near the islands. The general pattern is quite similar to the results in the chapter 4 when the Lagrangian method is adopted although the Eulerian method could detect a higher number of eddies.



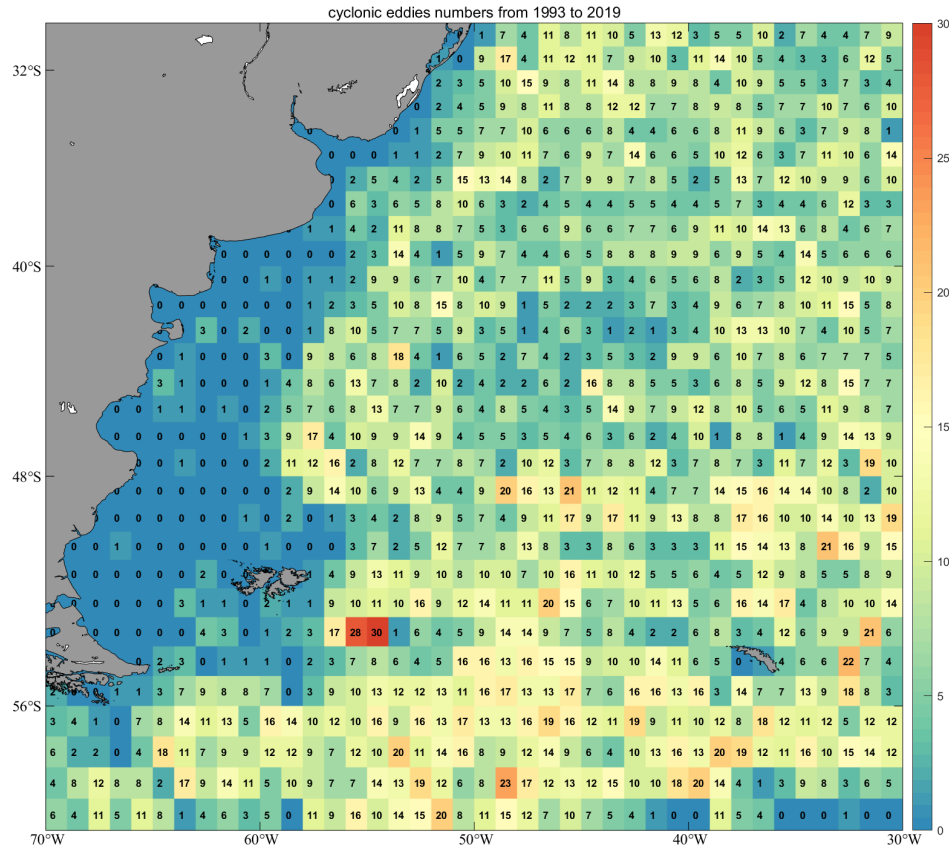


Figure 3.2: Cyclonic eddies numbers from 1993 to 2019

eddies with lifetimes longer than 30 days. In order not to overlap the trajectories with each other, only one-tenth of the total eddies are selected and plotted on the map.

From figure 3.5 , the observed temporal distribution of Eulerian eddies suggests that about 200-300 eddies would be generated in the Argentine Basin each year and the number of eddies decreases a little bit in recent years. Eddies number distributes unevenly in the four-season: in summer, more eddies would appear and fewer eddies would be generated in winter. This pattern is similar to the results found in chapter 4. The number of cyclonic eddies outweighs that of anticyclonic eddies by about 5%.

The radius of Eulerian eddies is about 70 km, and anticyclonic eddies are a little bigger than

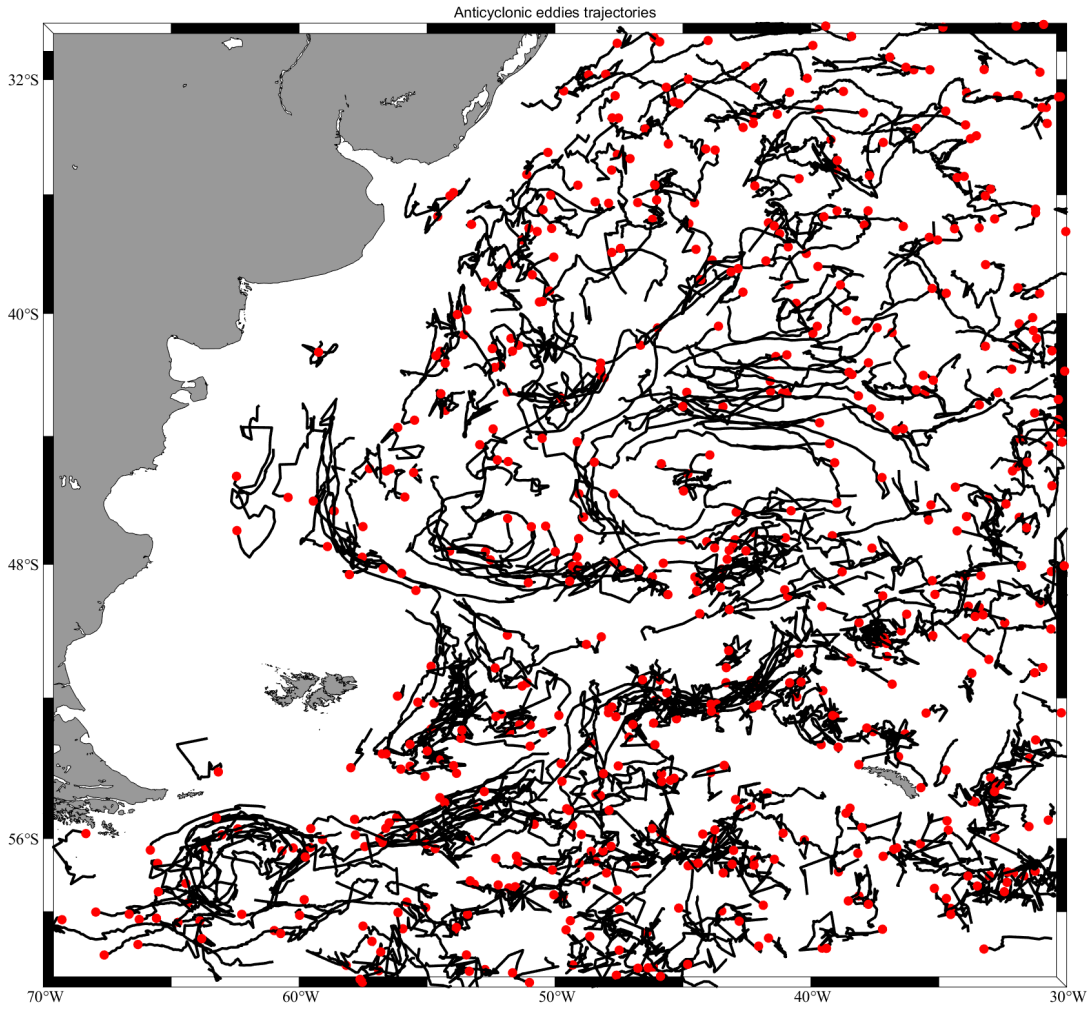


Figure 3.3: Anticyclonic eddies trajectories from 1993-2018

cyclonic ones. The result is about twice as large as the Lagrangian eddy, which implies that Eulerian detection method may outweigh coherent transport carried by oceanic eddies and the outer part of Eulerian eddies was not so robust.

Figure 3.7 and 3.8 show the life estimation of Eulerian eddies, eddies with life estimation ranging from 30 to 60 days occupies 61% of the entire number of vortexes while eddies with lifetime shorter than 30 days only account for 8% and eddies with life-range over 180 days only takes up 1.5% (1.6% in cyclonic eddies and 1.4% in anticyclonic eddies). The most long-living eddy

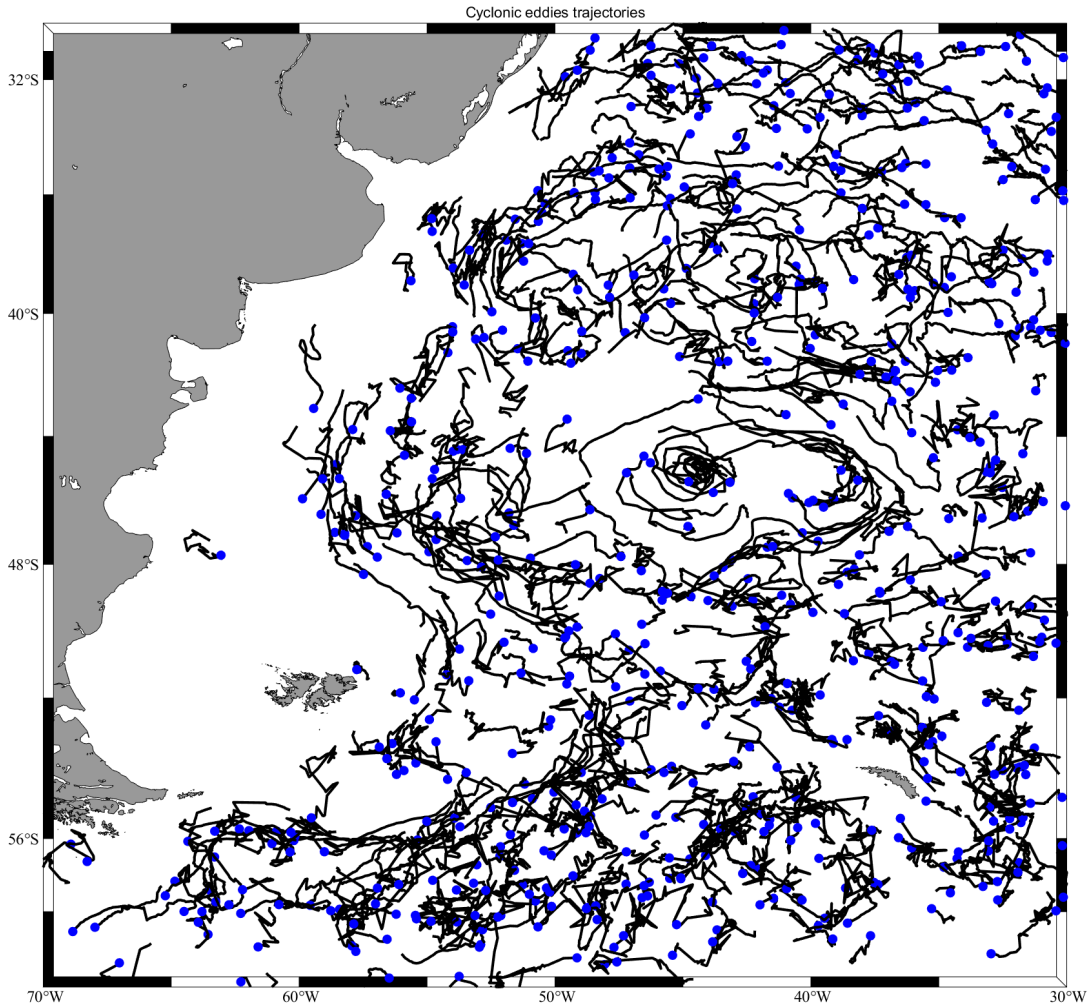


Figure 3.4: Cyclonic eddies trajectories from 1993-2018

lasted for 308 days. Thus, choosing 30 days as the coherent time for LAVD methods is convincing.

3.3 Comparison of Lagrangian and Eulerian methods

Since we adopt different methods to detect eddies, it is necessary to test the robustness of the results.

Search through the whole eddies dataset, we have found an Eulerian eddy that originated from

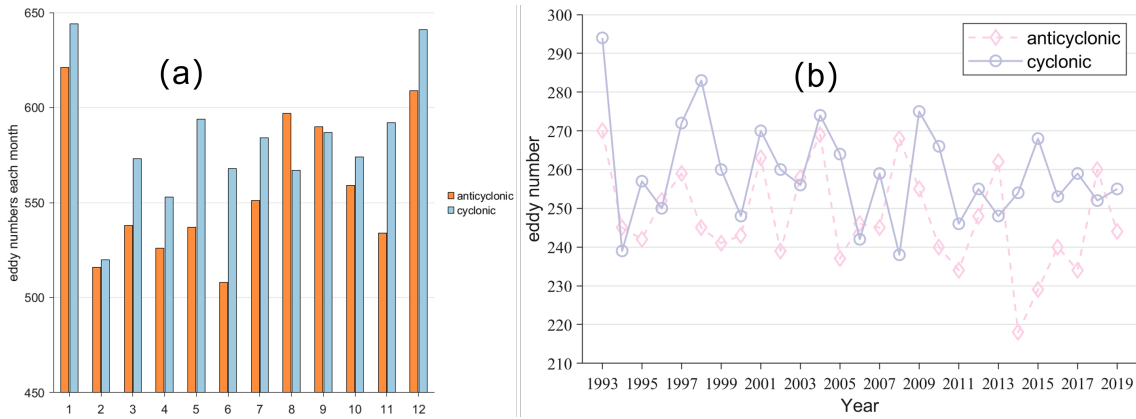


Figure 3.5: Monthly and annual volume change characteristics of Eulerian eddy

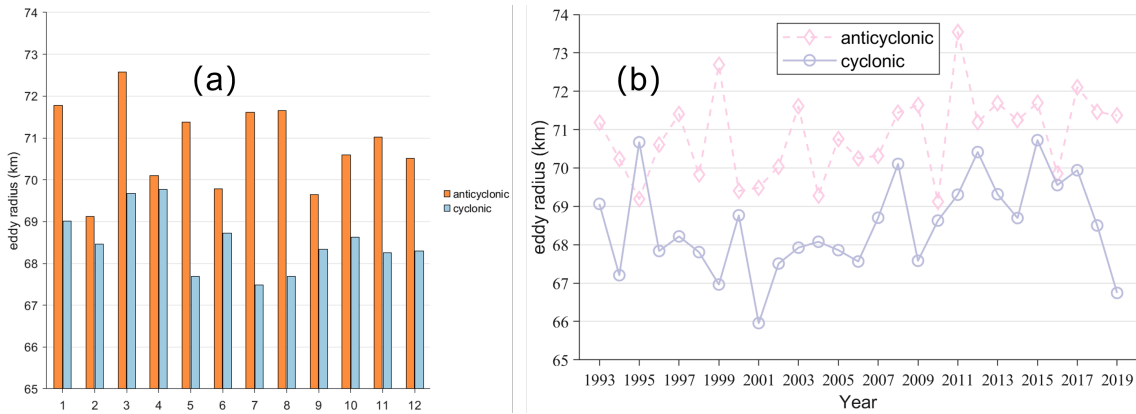


Figure 3.6: Seasonal and annual variation of Eulerian eddy number and radius

04-Aug-2006 and lasted for 140 days and the corresponding Lagrangian eddy has $t_0 = 2014 - 09 - 01$ and a coherent time of 120 days.

Figure 3.9 shows the evolution process of this selected vortex (x label represents the longitude and y label represents the latitude). In the figure, the coherent Lagrangian eddy part is marked in red, the blue dots represent the area enclosed by the Eulerian eddy, and the black ring shows the particle outside of the Eulerian eddy. We release the particles and find that the Eulerian eddy could maintain the overall shape in the first 15 days and then the outer part of the Eulerian eddy would deform and stretch in the evolution process. After 70 days, two fluid arms are flung from the core of the Euler vortex and 100 days later, only part of the blue particle is still inside the

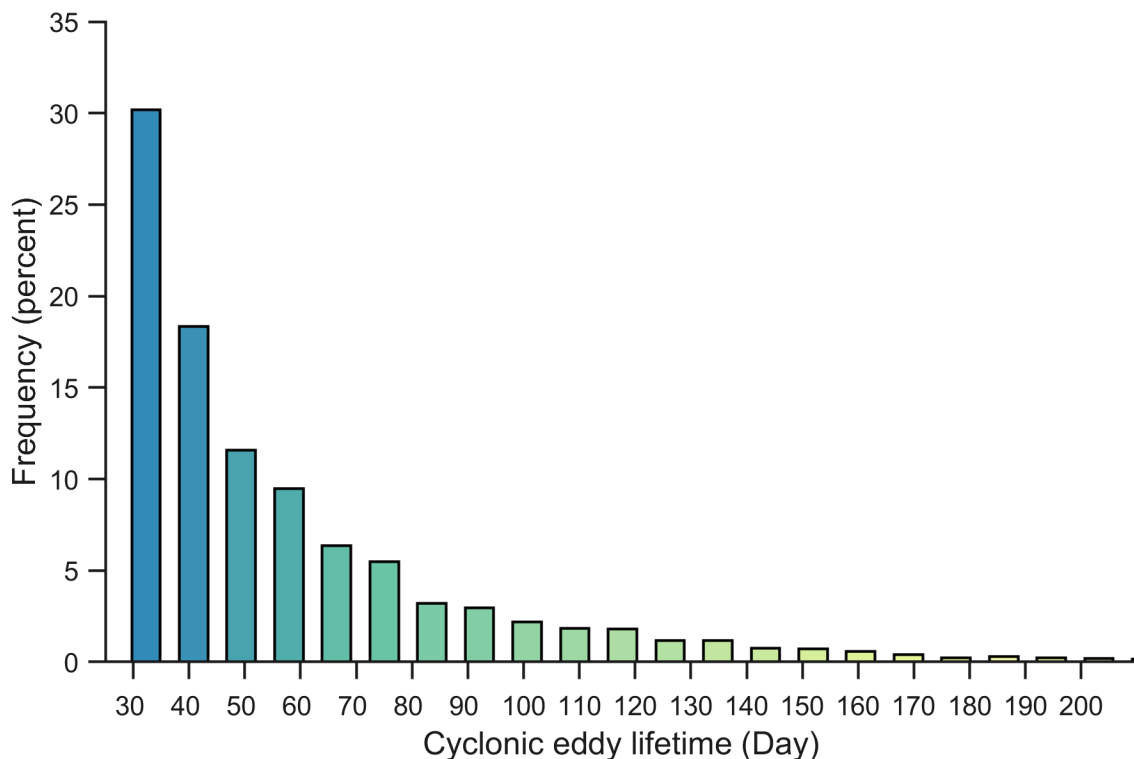


Figure 3.7: Cyclonic Eulerian eddy lifetime Frequency

Eulerian vortex. However, the LAVD Lagrangian eddy still maintains the main body and tracks almost all of the particles inside although the shape of the vortex changes a little bit.

Lagrangian eddies-detecting algorithms, thus, provide a convincing path to estimate eddies' number, size and carrying capacity for transporting a large amount of waters and particles both in oceanic model data and observational data.

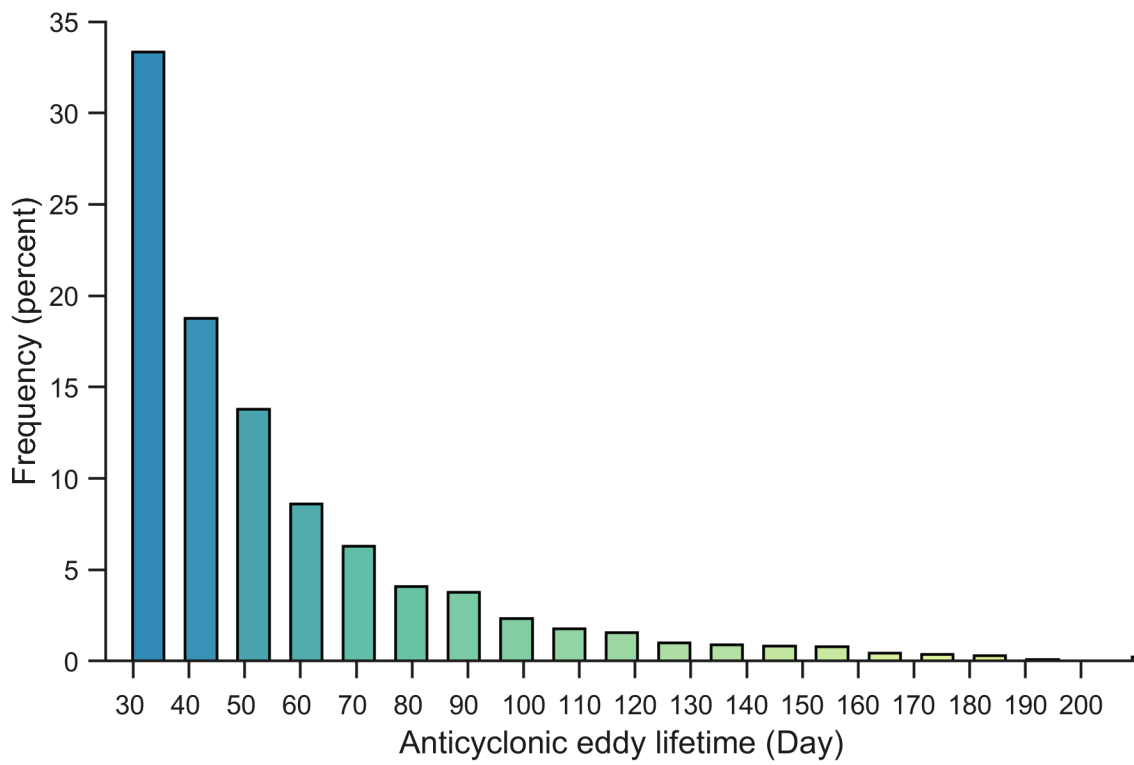


Figure 3.8: Anticyclonic Eulerian eddy lifetime Frequency

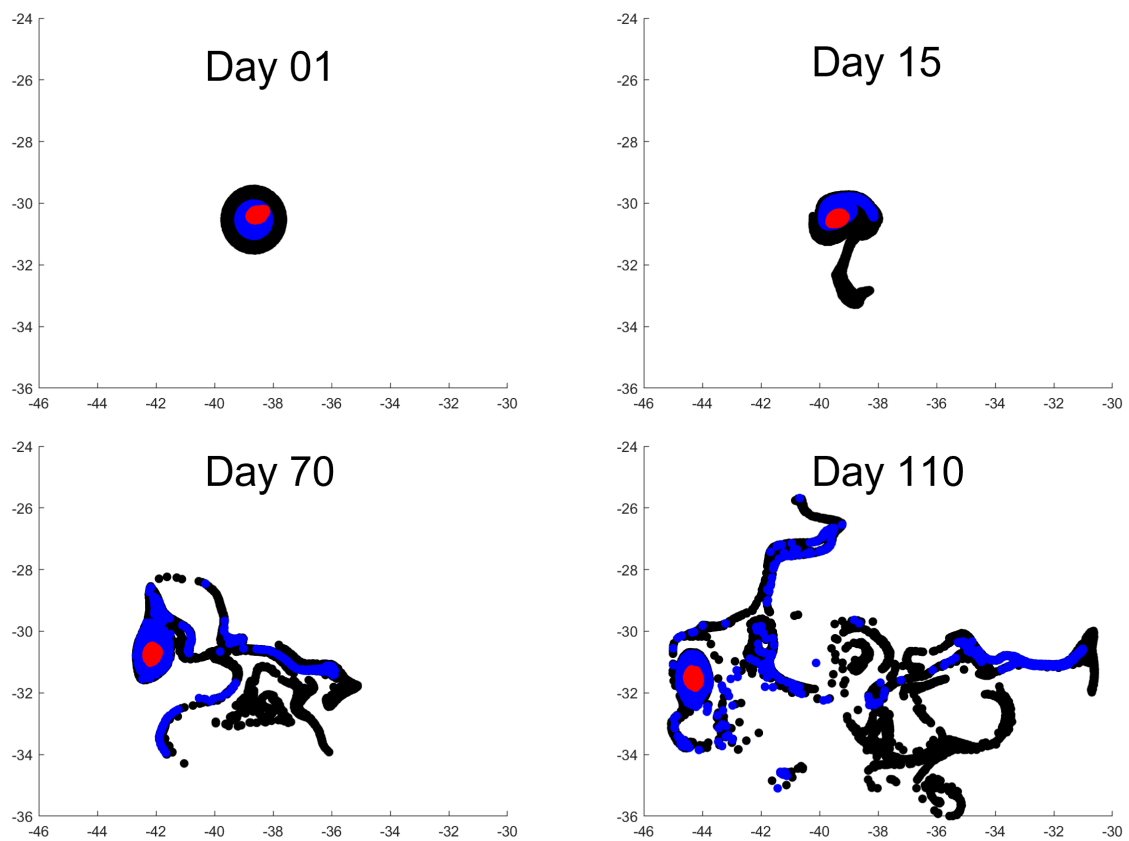


Figure 3.9: Evolution of one elected eddy

3.4 Conclusion

In this chapter, we use SSHA Eulerian method to detect eddies in the same research area and research period. We have several findings as concluded below:

- 1) The general appearance rules of the Eulerian eddy are quite the same as the Lagrangian eddy.
- 2) Eulerian eddies tend to have a bigger size and the number of eddies counted using the Eulerian method outweighs the number in LAVD research.
- 3) A case study of one long-living eddy suggests the robustness of the Lagrangian coherent eddy's transport capacity.
- 4) 30 days may be a reasonable choice for the detection period for oceanic eddy.

CHAPTER 4

EDDIES FEATURES ANALYSIS

In this chapter, we present statistical results of coherent Lagrangian eddies using LAVD method.

4.1 Eddies statistics

This chapter includes a set of figures showing census statistics about the eddies detected and tracked by applying LAVD method to AVISO dataset. Over the period of 1993-2019, 6212 coherent eddies with radius larger than 20 km and coherence time of 30 days were detected.

The figure 4.1 shows the monthly and yearly variation patterns of the eddy number. From the figure, we could infer that the number of eddies distributes unevenly in four seasons and shows a trend of increasing from 1993 to 2019. The average number of eddies per month is about 20 and it ranges from 10 to 40. Eddies' number rises to 41, and peaks in December 2014. The months with the fewest eddies were Feb 2000, Apr 2007, Jun 1994, and Oct 2010, and only 10 eddies were detected in those months as shown in section (c) of the figure 4.1.

In December, around 600 eddies were detected from 1993 to 2019 while only 452 eddies were detected in June. Seasonal change of eddy number shows that eddy number peaks in summer, decreases rapidly, and reaches the minimum value in winter. From (b) part of the figure 4.1, we could come to a conclusion that eddies number increases over the last three decades, showing a

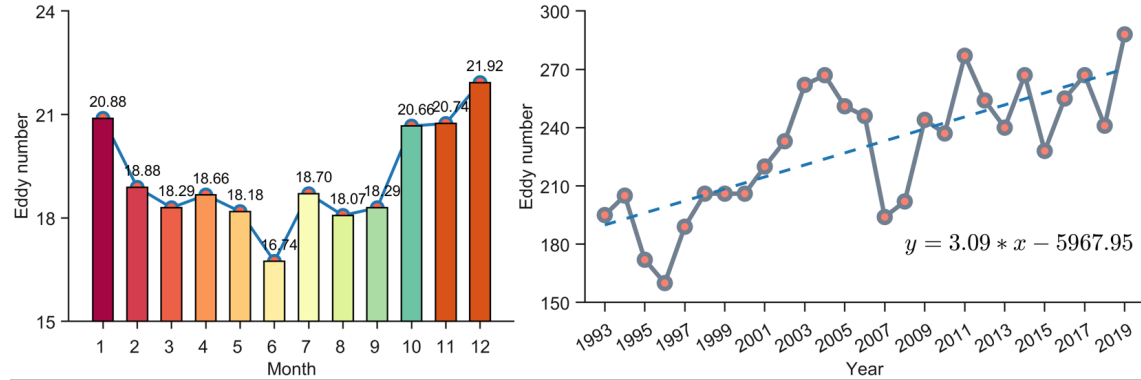


Figure 4.1: Eddy number per month and per month

hint of how global warming would increase the instability of the upper ocean and the increasing rate is 3/year.

The average eddy radius is 32.98 km and the standard deviation is 11.31 km. From the eddy radius histogram as shown in section (c) of the figure 4.2, we could infer that most of the eddies fall within the range of 20-30 km. The frequency of eddy radius decreases exponentially with increasing radius. From section (b) of the figure 4.2, eddy radius does not show an upward or downward trend year by year. Eddies that were generated in 2019 show an average maximum value of 34.41 km while eddies reached the minimum value (31.3 and 31.5 km) in 1996 and 1997. The monthly change of eddy radius shows a minimum value in July and August and a maximum value in December.

Combining the information on eddy number and eddy radius, we may come to the conclusion that in winter, the number and radius of eddies will be reduced due to insufficient energy in the upper ocean.

The figure 4.3 shows how eddy's radius changes with latitude. From the figure, we could learn that eddies in high latitudes would tend to have a smaller radius, and eddies in lower latitudes would have a larger radius. We also calculated the stretching ratio between the initial eddy area

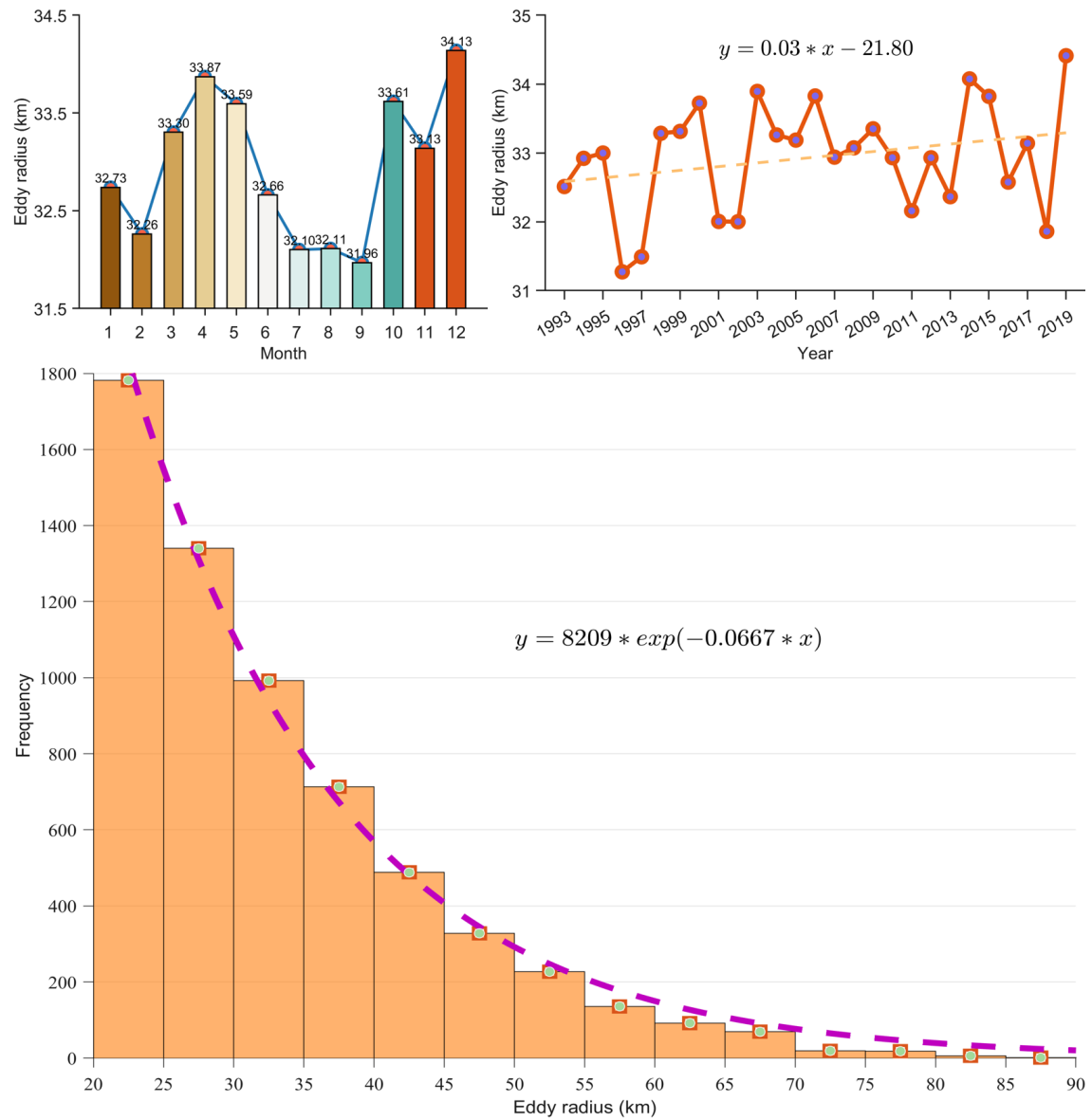


Figure 4.2: Eddy radius frequency distribution histogram

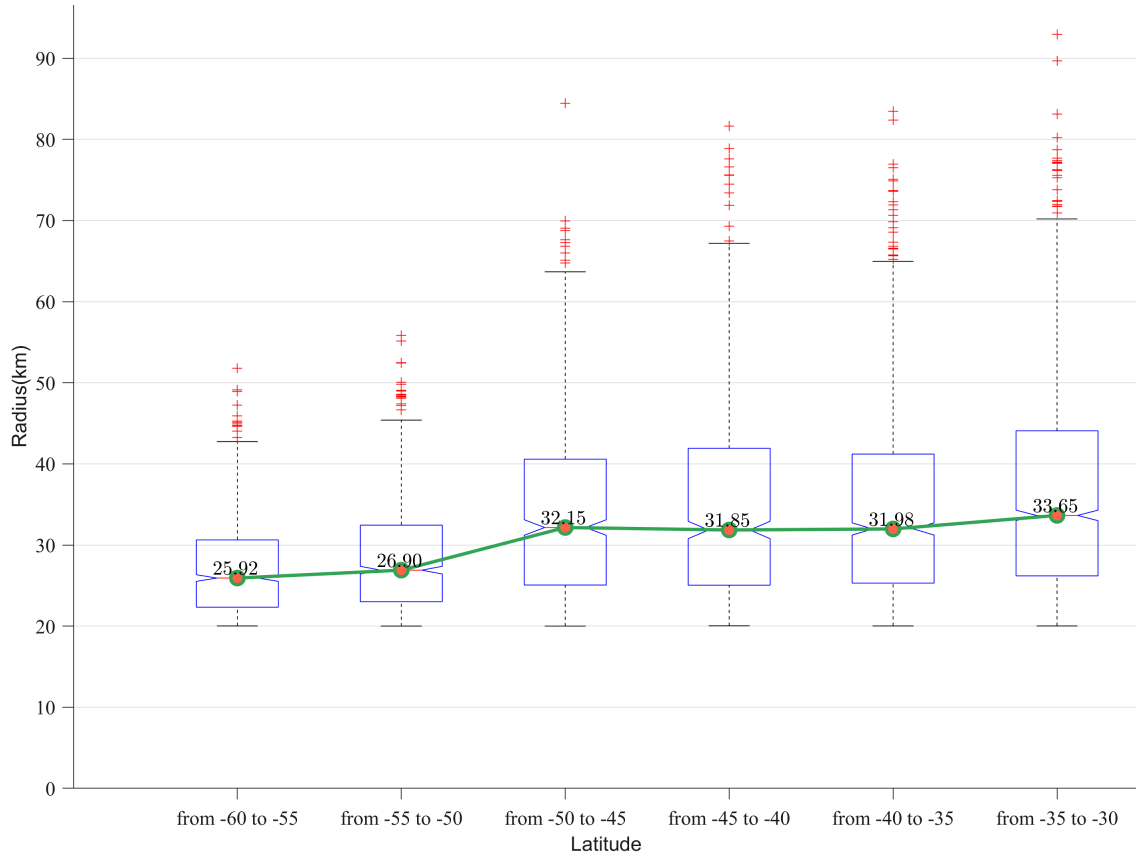


Figure 4.3: Relationship of vortex radius with latitude

and the final eddy area and the result is shown in figure 4.4. We infer that eddy would have an inclination to be compressed during the coherent period and the ratio reduces to 0.85 from -55° S to -60° S, which suggests that the LAVD method may not be so robust in high latitude.

The figure 4.5 demonstrates how eddy propagates in the coherent period. The average propagation speed of the eddy is approximately 5km/day and eddies have the largest propagation speed (about 6.5 km/day) in the middle latitude ranging from -50° S to -40° S. However, the propagation speed will reduce to about 3.6 km/day in higher or lower latitude. There are many outliers for the vortex transport speed in the figure 4.5, which implies the nonlinear effects and causes the vortex moves disorderly. What is more, in most of the cases, the eddy's zonal transport velocity outweighs its meridional component. As shown in figure 4.6, the maximum value

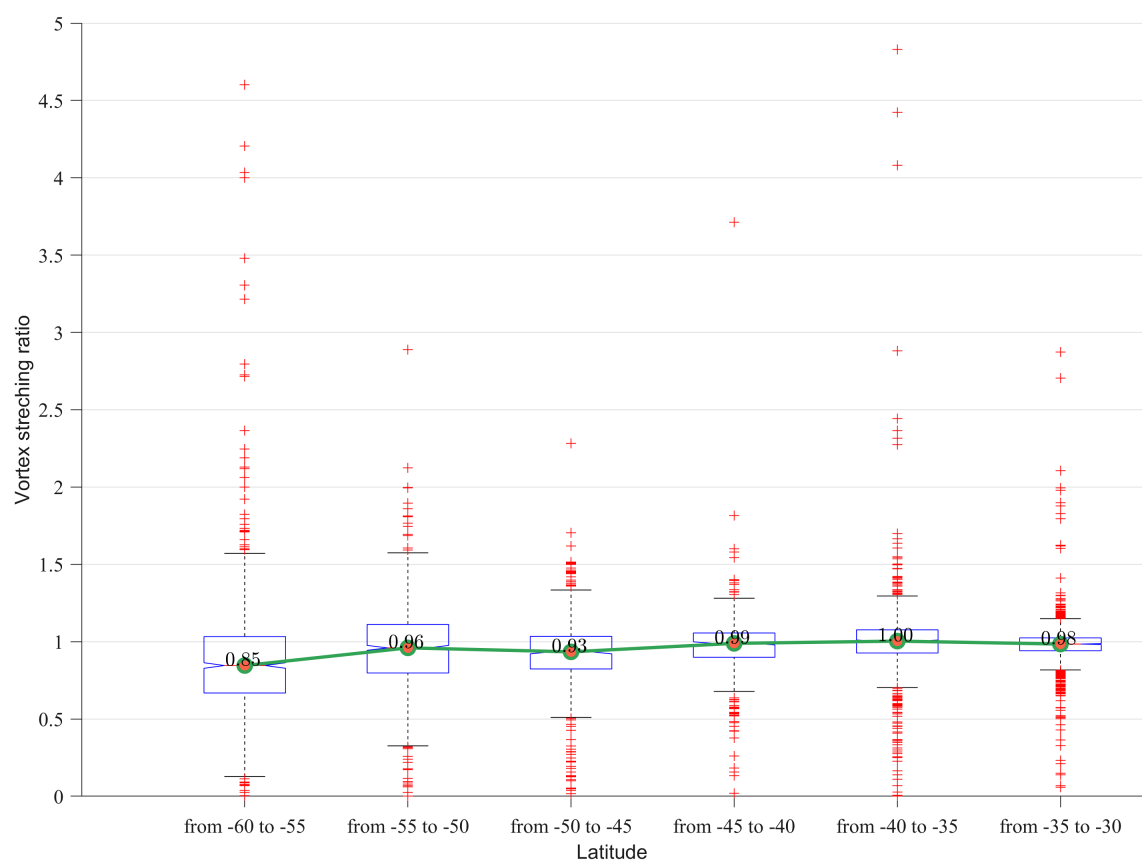


Figure 4.4: Relationship of vortex stretching ratio with latitude

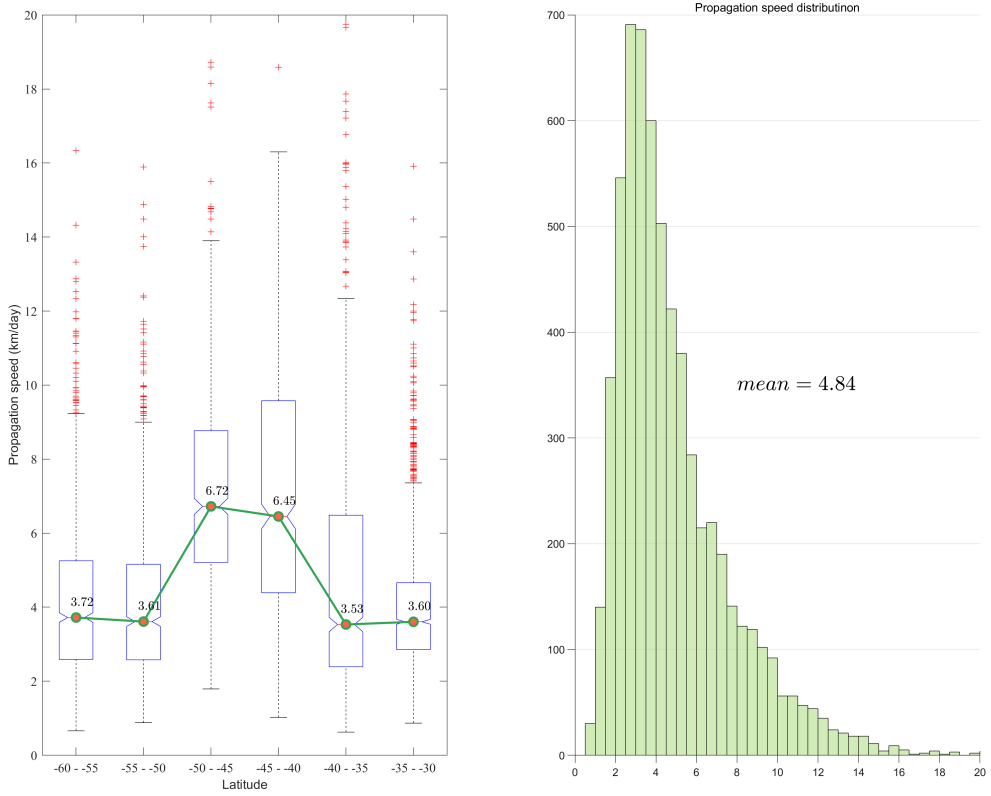


Figure 4.5: Relationship of eddy velocity (km) with latitude

of zonal velocity is 5.61 km/day near -45°S latitude while the maximum value of meridional velocity is 4.88 km/day at latitudes between -47°S and -50°S . They both show the trend of maximum at intermediate latitudes and decreasing at both low and high latitudes.

The geographical distribution of eddies from 1993 to 2019 is given in the figure 4.7. Among the 6212 vortices, 3336 of them are cyclonic eddies while 2876 of them are anti-cyclonic, which means that cyclonic vortices outweigh anticyclonic ones by about 15%. Along the southwest edge of the Argentine Basin, the majority of eddies were cyclonic eddies. Eddies distribute evenly in the Southern Ocean region, while there are more eddies in the northeast part of the Argentine Basin. There is a vortex "vacuum" zone in the center of the Argentine Basin, with

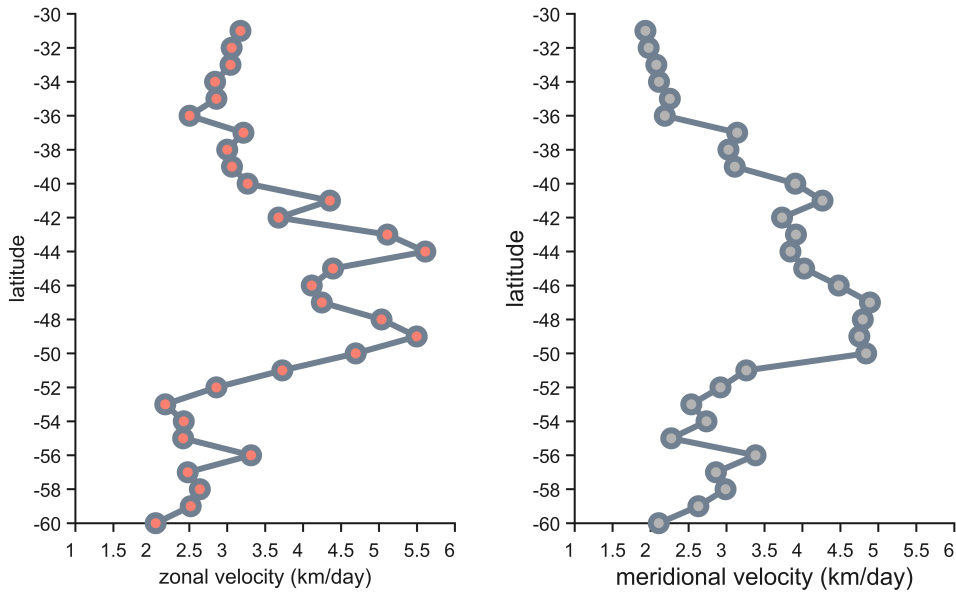


Figure 4.6: Relationship of zonal and meridional velocity with latitude

only a few vortices remaining there. In the shallow water areas near South America Continent, we detected more anticyclonic vortices. There are few eddies detected in the coastal region since the deviation of altimeter data near the coastline is rather high due to the influence of tides and coastal waves. In the water regions connecting the Southern Ocean and Argentine Basin, eddies distribute in a striped pattern.

The figure 4.8 shows annual variation and monthly variation of eddy number and vortex radius of cyclonic and anti-cyclonic eddies. Anti-cyclonic eddies have distinct seasonal variations while seasonal number differences of cyclonic eddies are small. In all months, the number of cyclonic vortices is higher than the anti-cyclonic ones. The average number of anti-cyclonic eddies appearing in June is 7.59, which is the lowest in all months. Anti-cyclonic eddy number reaches the minimum value in winter and it increases slowly and reaches a maximum in winter. Annual variation characteristics of vortex numbers tell us that in most of the years, cyclonic eddy numbers outweigh anti-cyclonic ones while the opposite rule was observed in 1995 and

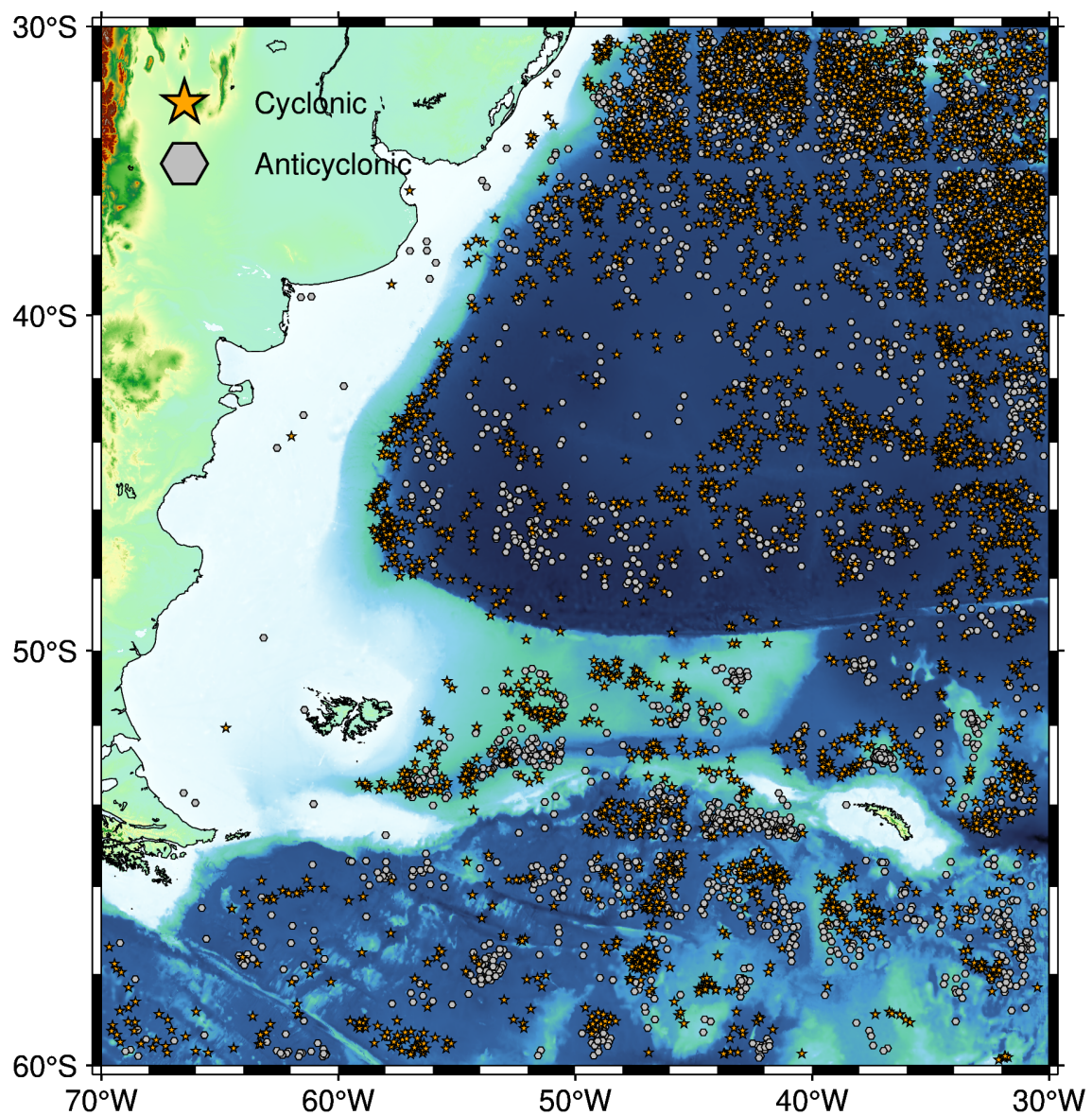


Figure 4.7: Eddy polarity distribution map

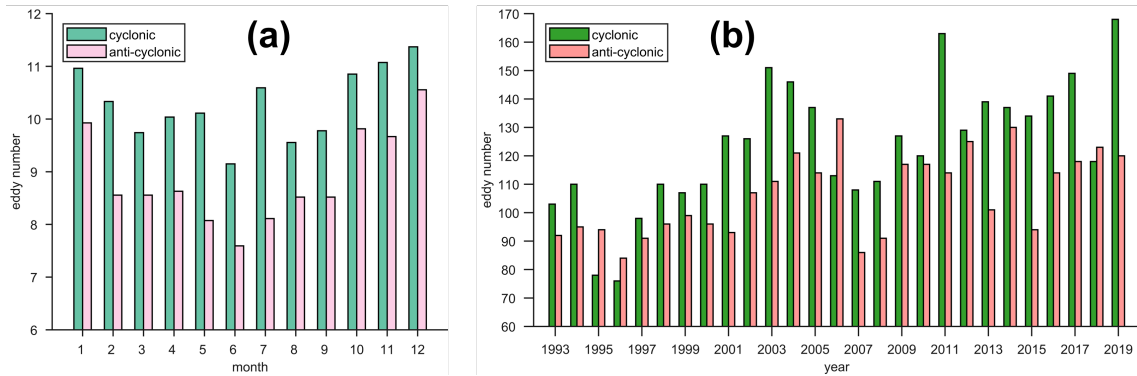


Figure 4.8: Monthly and annual patterns of eddy number of different polarities

1996. An average of 124 cyclonic vortices and 107 anti-cyclonic eddies are generated each year. Both the number of cyclonic eddies and anti-cyclonic eddies would increase, and the increasing trend of cyclonic eddies is more obvious. The maximum number of annual cyclonic eddies found in the Argentine Basin is 168 in 2019 while the maximum number of annual anti-cyclonic eddies is 133 in 2006.

Figure 4.9 shows how vortex polarity affects vortex size. Before 2010, the diameter of the anticyclonic vortex was more extensive than that of the cyclonic vortex. Since 2007, the radius of cyclonic vortex began to grow and has become bigger than anti-cyclonic ones. From the figure, we could learn that different types of eddies have different seasonal patterns. The average monthly minimum radius of cyclonic eddies is 31.52 km in September while the minimum monthly radius of anti-cyclonic vortices is about 32 km in June. They both show maximum value in December.

In Figure 4.10, we compared eddies' initial position and final position from 1993 to 2019 and the figure shows the direction of eddy propagation. About 59% of the eddies would travel northward, and only 41% would travel southward. Anticyclonic vortices are more inclined to transport to the poles. In the east-west direction, about 63% of the eddies travel westward, and

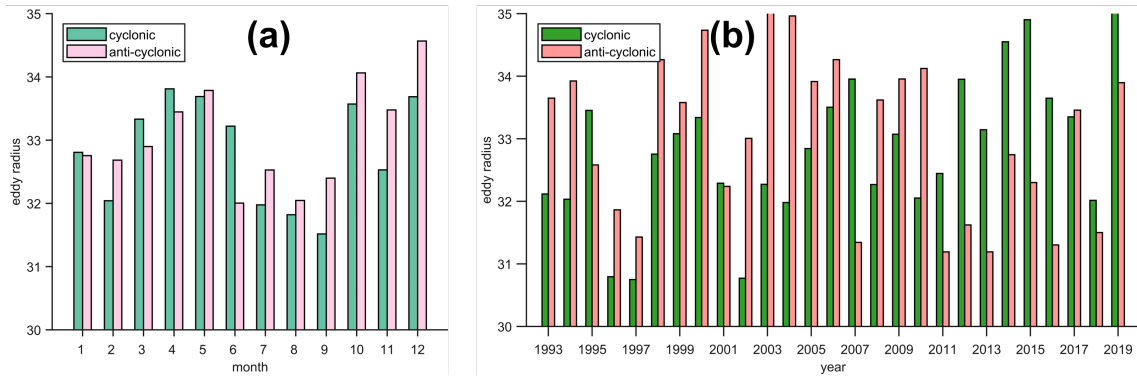


Figure 4.9: Monthly and annual patterns of eddy radius of different polarities

only 37% of them travel to the east.

From the map, we could learn that even in the northern part of the Argentine Basin which is affected by the southward Brazil Current, most of the eddies would tend to travel northward, which suggests an opposite direction of the mean flow and eddy flow. Along the border connecting the shallow water region and Argentine Basin, we could learn that eddies in the northern part of the border have an inclination to travel southward and eddies in the southern part have a trend to travel northward. This is coincident with the southward Brazil Current and northward Malvinas Current. In the middle of the Argentine Basin, eddies' travel pattern agrees with the Zapiola Anticyclone.

In the Southern Ocean region, most of the observed eddies travel eastward because of the Antarctic Circumpolar Current. On the northern part of the Argentine Basin, the majority of the eddies propagate westward. In the center of the basin, because of the Argentine Gyre and branch of the Brazil Current, we could see that at the southern edge of the basin, eddies would tend to move eastward while eddies would move to the west in the middle of the basin.

Figure 4.11 shows some cases study of the eddies transport path. As shown in section (a) of figure 4.11, a cyclonic eddy propagates westward in the center of the Argentine Basin. Section

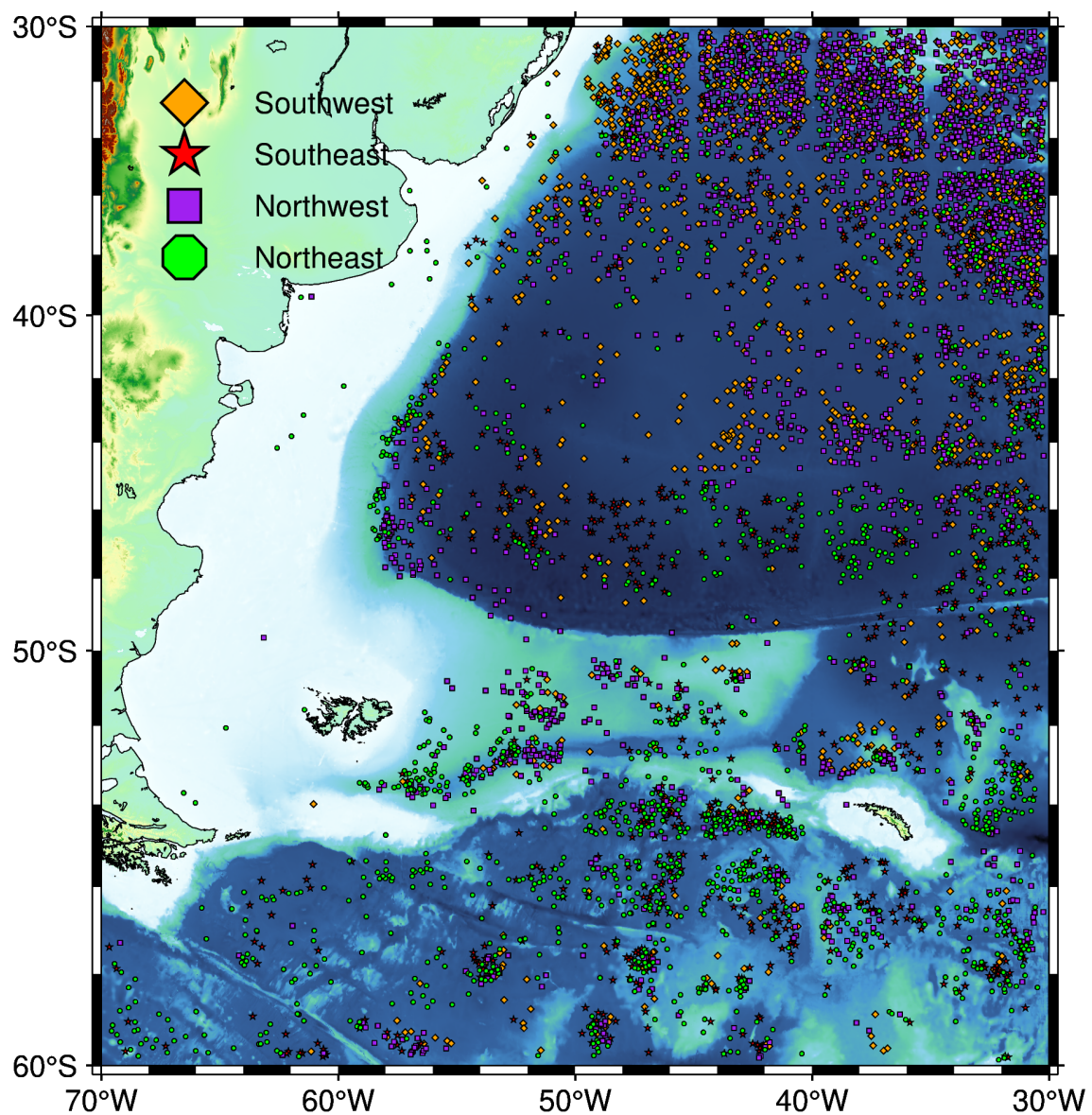


Figure 4.10: Eddy travel direction map

b shows an anti-cyclonic eddy on the southern border of the basin and its travel direction is to the southeast. In Section C of the figure, one cyclonic eddy near South Georgia and the South Sandwich Islands goes north and it lost its coherence strongly during the last ten days of transport. Section d of the figure depicts a typical vortex going southward along the South American continental slope, the direction of which is the same as the mean flow thus, a considerable number of vortices are also transported this way.

4.2 Eddies coherence time

In Chapter 4.1, we set the coherent time of 30-day and detect 6212 coherent eddies in the study period from 1993 to 2019. However, the properties of the coherent eddy are affected by the selection of time interval to a large extent [59, 60].

In the context of the Eulerian detection method (SSHA), the vortex life cycle is defined as the time period of the process of a vortex from birth to death [61, 62]. According to the previous research, the life cycle of a vortex varies from 4 weeks to 16 weeks and the average life cycle is about 8-9 weeks.

The result is shown in figure 4.12. From the figure, we could learn that there is a rapid decrease in eddy number when the coherent period is less than 90 days, but the trend slows down after 90 days, which means that an eddy with a life cycle larger than 90 days would tend to survive longer. We could also conclude that eddies with a coherent period of 90 days have the largest radius which suggests that an eddy with a larger radius, magnitude, and intensity will survive longer. 60-day eddies' radius is smaller than 30-day eddies' and 120-day eddies' radius is smaller than 60-day eddies', which shows that the time period has an impact on vortex co-

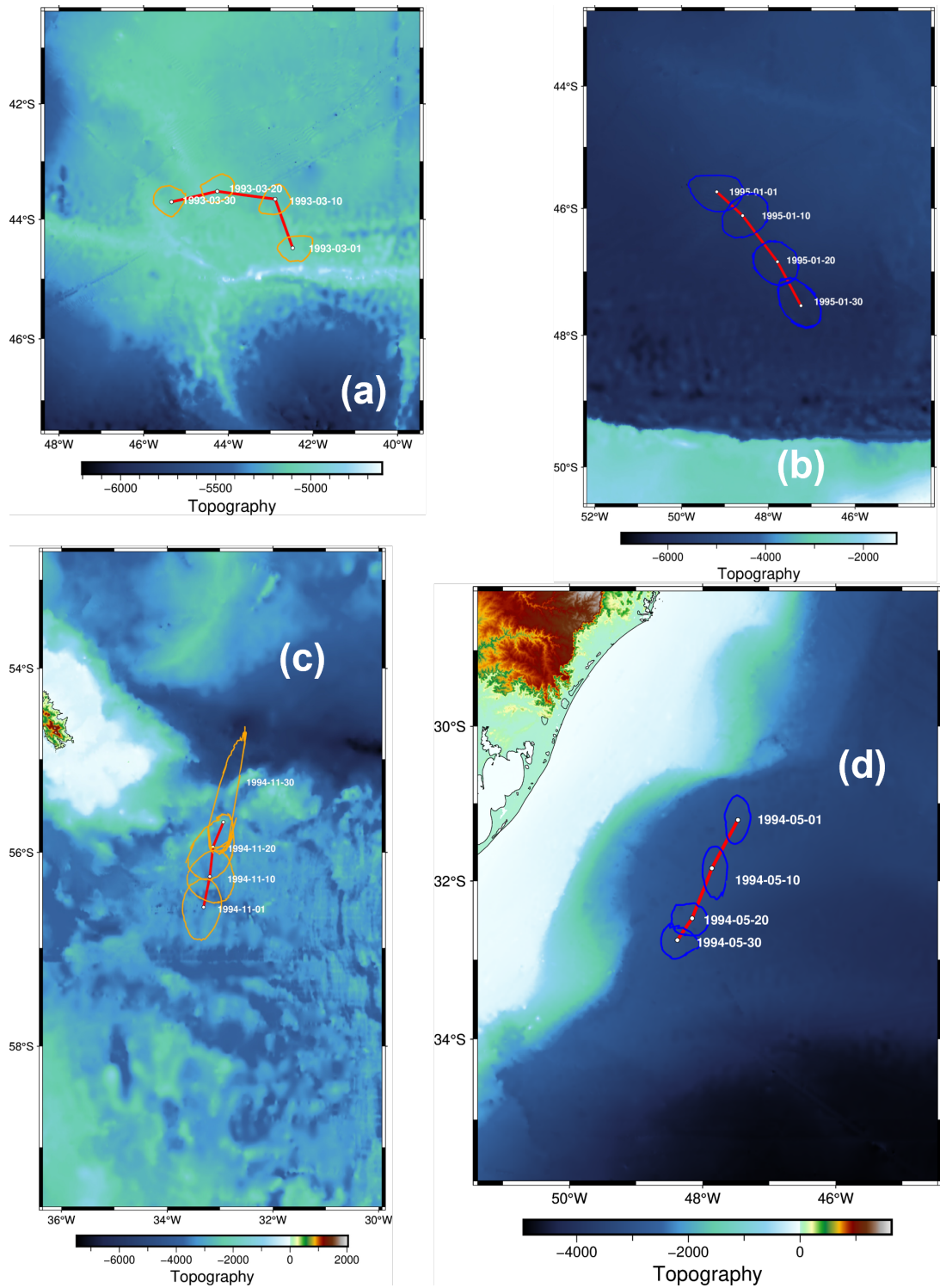


Figure 4.11: Some vortex examples (orange for cyclonic eddy and blue for anti-cyclonic eddy)

herence and if we track the eddy exceeding the period Δt , the outer part of the eddies would be deformed, stretched into filaments, and finally lose coherence.

From figure 4.13, we could learn that anticyclonic eddies tend to have larger coherent time. When the coherence period is 30-day, anti-cyclonic eddies only occupy 46% of the total eddy number; while the proportion raise up to 64% when the coherent interval is 120-day.

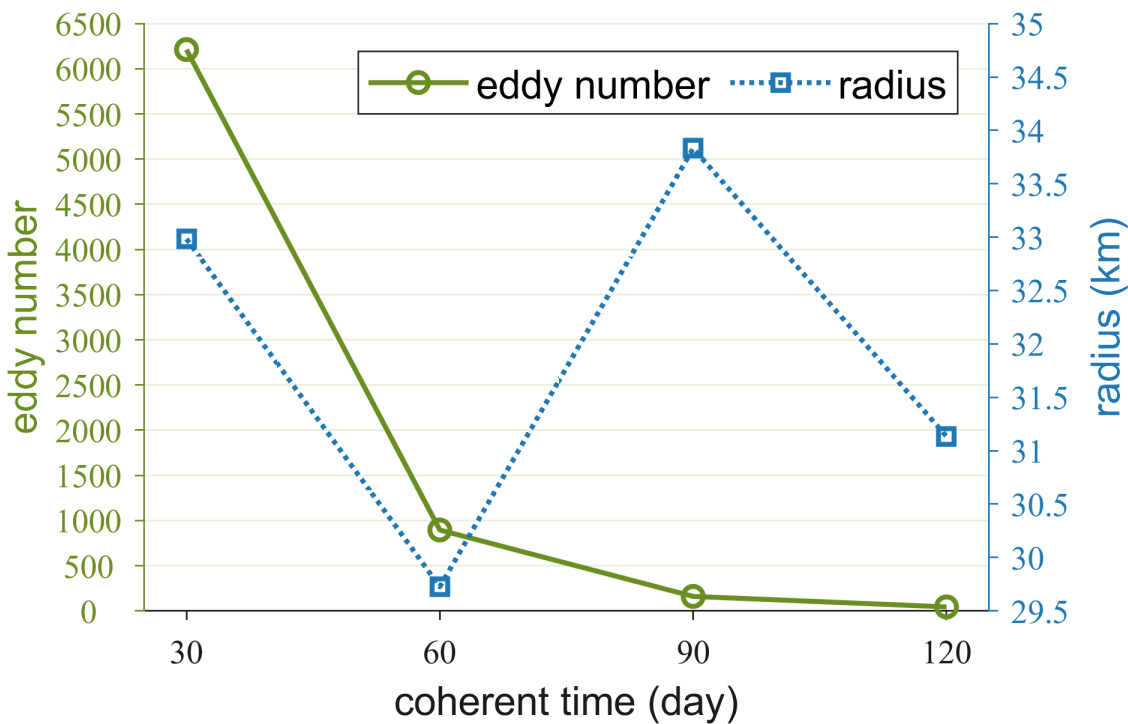


Figure 4.12: Eddy properties and their relationship with coherence time

Figure 4.14 shows three detected eddies with a coherent time of 120 days. In section (a) of the figure, the coherent time of the anti-cyclonic eddy originated in January 1998, the anti-cyclonic eddy shown in section (b) of the figure stemmed from September 2006 while the cyclonic eddy in section (c) was calculated using $t_0 = \text{September} 2019$. In the figure, the initial position is marked with a black circle and the final position is marked in orange; anti-cyclonic eddy is indicated in red while cyclonic eddy is indicated in blue. They all show a westward propagation

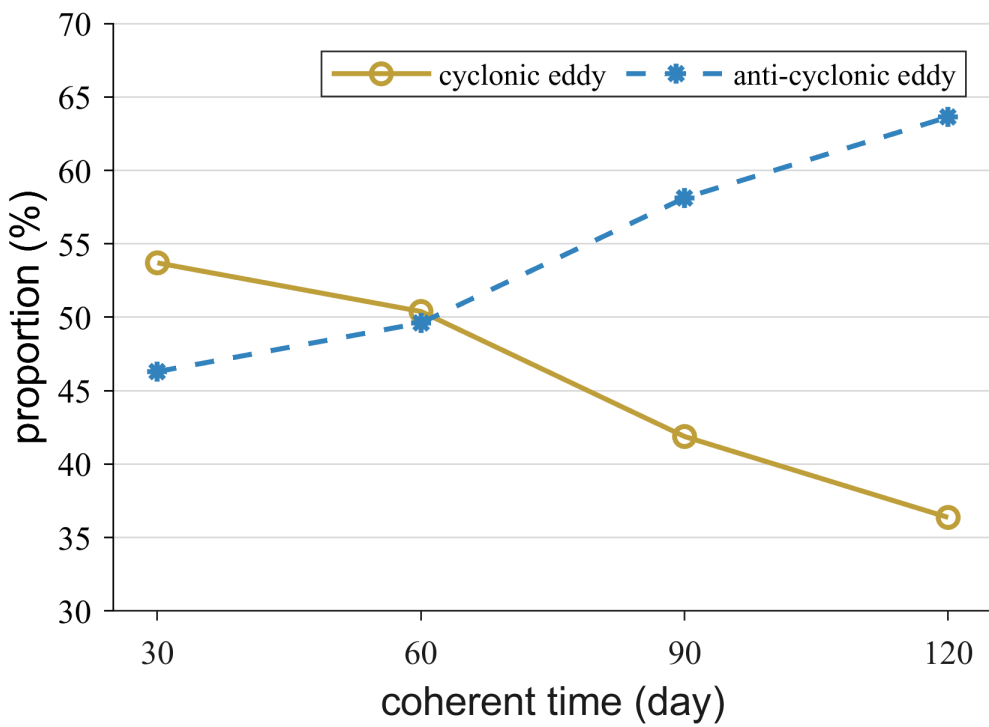


Figure 4.13: Eddy type proportion map

trend, carry water masses from the east to the west boundary, and finally the sea surface signal piles up at the west.

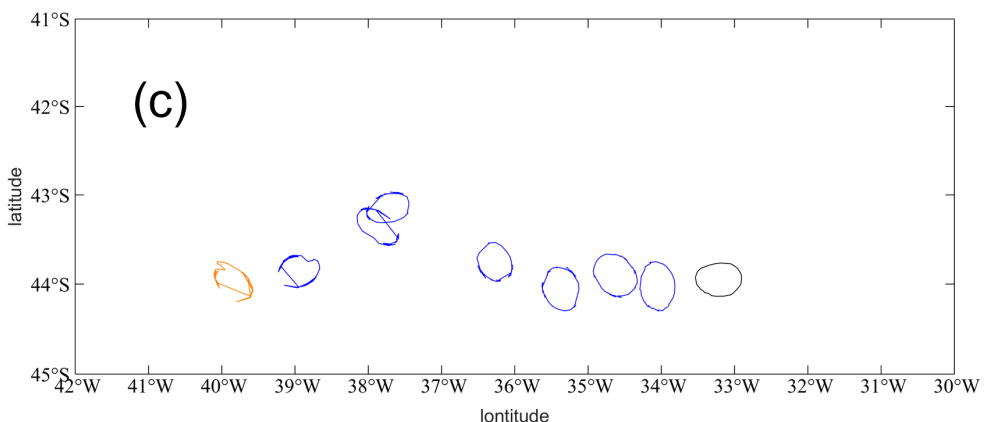
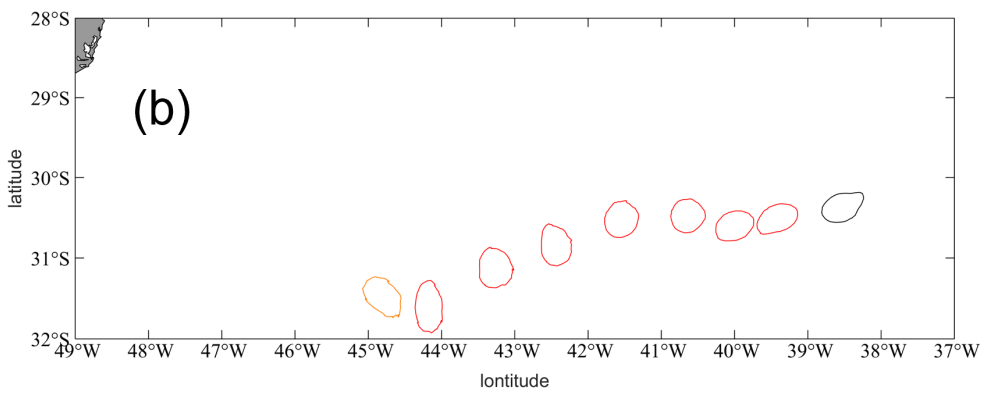
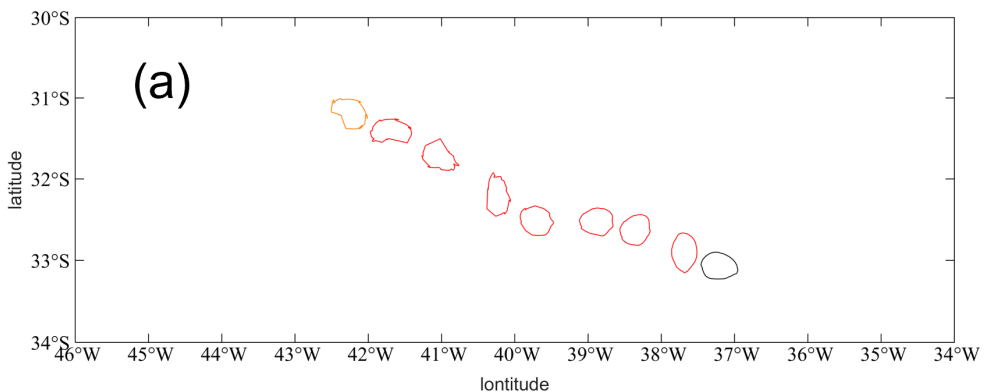


Figure 4.14: Trajectories map of three 120-day vortices

4.3 Conclusion

According to the criterion of the LAVD method, we have detected a total of 6212 coherent vortices, including 3336 cyclonic vortices and 2876 anticyclonic vortices from 1993 to 2019.

There is an upward trend of eddies number. From the statistical results, there are obvious seasonal changes in the generation of anticyclonic vortices, which are more in spring and summer and less in autumn and winter.

Analysis of regional eddy statistics reveals hot spots of generation in the northeast part of the Argentine Basin and reveals the limitations of the LAVD method in high latitude regions and coastal shallow waters.

Lots of eddies have been observed in the southwest part of the Argentine Basin where Brazil Malvinas Confluence gives rise to baroclinic instabilities. The Center part of the Argentine Basin is associated with an eddy-free zone. The northern part of the Argentine Basin and connecting region between the Southern Ocean and the Argentine Basin are also the hot-spot of the oceanic eddy.

Eddies' radius decrease when the latitude is higher and the propagation speed is the largest in the middle latitude.

Vortex polarity has an effect on vortex properties: anticyclonic eddies are more stable and tend to have larger coherent time.

CHAPTER 5

THREE-DIMENSIONAL EDDIES STRUCTURES

In this chapter, we present statistical and descriptive results of the vertical structures of oceanic eddies from 2013 to 2018 from the SOSE model dataset. Vortex penetration depth, radius distribution in each layer, and different patterns of cyclonic and anticyclonic eddies are discussed here.

5.1 Introduction

Although a lot of studies focusing on surface altimetry have investigated the horizontal properties of the oceanic eddies, very few of them can answer the questions of what the vertical profile of the eddies looks like and how they will affect the estimate of the volume transport. What is worst, some of the previous studies put forward prior assumptions about the vertical shape of the eddies and the mathematics-derived result may not be so robust. Some researchers want to deduce the vertical structure from Argo float data. However, time lag between the time when a float reaches the surface and the time when it reports its location with the Argos positioning satellite, and positioning errors limited by the accuracy of the Argos positioning system may raise the uncertainty of the identification[63].

Most of the past research or publications only focus on the two-dimensional plot of oceanic eddies, partly because only the ocean surface observations are available, and partly because the

magnitude of vertical velocity is three-orders less than the horizontal velocity, yielding a lot of noise to produce three-dimensional analysis and construct the three-dimensional structure. Sparse distribution of the observational array can only capture a limited picture of eddies features and thus ocean model, which provides a three-dimensional panoramic view of the ocean, fills in the gap in our understanding of three-dimensional ocean state variable

One feasible solution is using Lagrangian tools such as drifts or Argo floats, with the hope that drifts are located around the eddy cores and the selected interpolation scheme is suitable to estimate the real oceanic state around the eddies.

Questions still exist about the three-dimensional structure of oceanic eddies: (1) how do the eddies extend in the vertical direction; (2) how do eddies enhance the stirring and coupling of the upper ocean and deep ocean.

There is great concern about the understanding gap between the surface eddies and deep eddies. The ocean is divided into three zones in the vertical direction: a well-mixed surface region, rapidly varying ocean subsurface thermocline, and the stratified ocean interior. The ocean surface and ocean interior, with distinct features and separated by the thermocline, set up the questions about the relationship between surface eddies and deep eddies. Some eddies are constrained only to the surface, some will extend to the deep sea, while others subsurface eddies show no sign of the surface height signal. Worse still, it is rather difficult to extract Lagrangian structures and elaborate their effect on mixing properties in unsteady 3-D flow due to the explosion of complexity [25].

5.2 3D structure construction algorithms for an eddy

In chapter 2.3, we show how to set up a computational process and detect eddy on the surface. Repeating the same process and using the flow field information at 42 layers in the numerical data, we could get the 3D structure of coherent eddy. As discussed in the previous paper, an eddy center would not drift by 1/4 of its radius when it goes down 50 m if it is still detectable [47].

Thus, the overall workflow of the detection would be as follows:

- 1) Compute the LAVD field in each depth layer and extract eddies from the surface layer to the other below layers following the same process in Chapter 2.
- 2) Group the extracted eddies according to their characteristics and then select eddies based on judging criteria “an eddy center would not drift by 1/4 of its radius when it goes down 50 m”.
- 3) If in the same depth level, more than one eddies were found, pick the vortex with the closest horizontal distance from the surface one.

5.3 Eddies penetration depth and three-dimensional shape type

To construct the vertical profile of the eddies, we use the velocity filed results generated from SOSE oceanic model. The horizontal resolution of SOSE dataset is $\frac{1}{6}^{\circ}$ and SOSE dataset has 41 layers in the vertical direction in total, covering variables from the surface to 5km in depth.

We have detected 732 eddies in the surface layer from 2013 to 2018 and 566 (77%) of them were found to have signals in the below layers and used to construct the 3-D structure in the research, which suggests an amount of about 25% of the eddies is quite shallow

From figure 5.1, we could find that about half of the eddies could still be detected at a depth of 2010 meters, about 20% of the eddies have depths ranging from 1500 m to 1800 m, and about 18% of them reach the depth of 1000m to 1500 m.

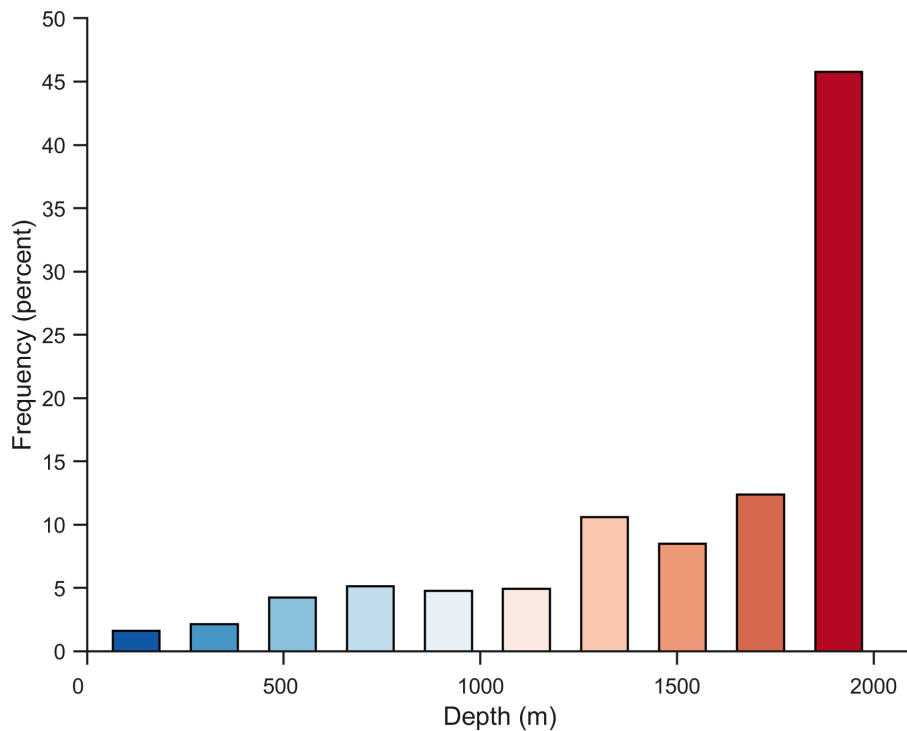


Figure 5.1: Histogram distribution map of vortex depth

Among all the 566 3-D eddies, about 52% of them (294) are cyclonic eddies and about 48% of them are anticyclonic ones. The maximum vortex radius of the cyclonic eddies is placed at depth of around 826 meters while the maximum vortex radius of the anticyclonic eddies centers at depth of 659 meters or so. The average value of the maximum depth of the cyclonic vortices is about 1679 meters and the mean value of the maximum depth of the depth extension

of anticyclonic eddies is 1496 meters. The above findings show us that cyclonic eddies tend to have a greater vertical extension and thus they have stronger transport capacity and could carry more volume of seawater.

According to existing papers, the eddy vertical shape of oceanic eddies could be classified into three kinds: eddies with the largest semidiameter on the surface like a bowl, cone-shaped vortices with the largest radius at the bottom layer, and lens-shaped eddies having the largest size in the middle [47, 64].

In the Argentine basin, all those three types of eddies were found and lens-shaped eddies are the majority: 72 of the detected eddies were bowl-shaped, 412 of them are lens-shaped and 82 of the eddies are cone-shaped vortices. The following figures from 5.2 to 5.4 show the vertical distribution of some selected eddies. Figure 5.2 illustrates three bowl-shaped eddies having a maximum radius on the surface and then decreasing towards the bottom. Figure 5.3 shows three eddies having maximum radius in the intermediate layer and then becoming smaller with increasing depth. In figure 5.4, eddies on the surface are the smallest, gradually get larger, and reach a maximum at the bottom. The vortex radius may be more stable in size in the intermediate layer.

5.4 Case studies of oceanic eddies

Figure 5.5 shows the vertical slice of salinity field and radius distribution of a cyclonic coherent eddy with $t_0 = 2014 - 01 - 01$. We could find that the subsurface vortex radius has a maximum value of and the eddy's size changes dramatically on the surface. In section (a) of the figure 5.5, each slice represents the salinity distribution in each depth layer. The minimum value of the

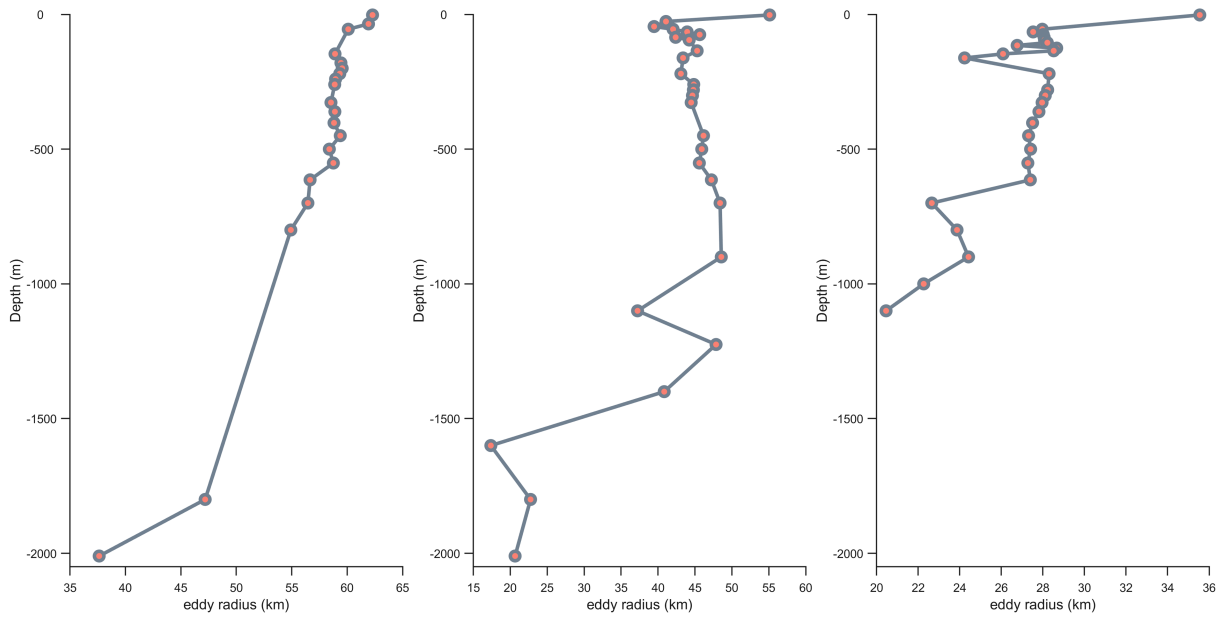


Figure 5.2: Three examples of bowl-shaped eddies

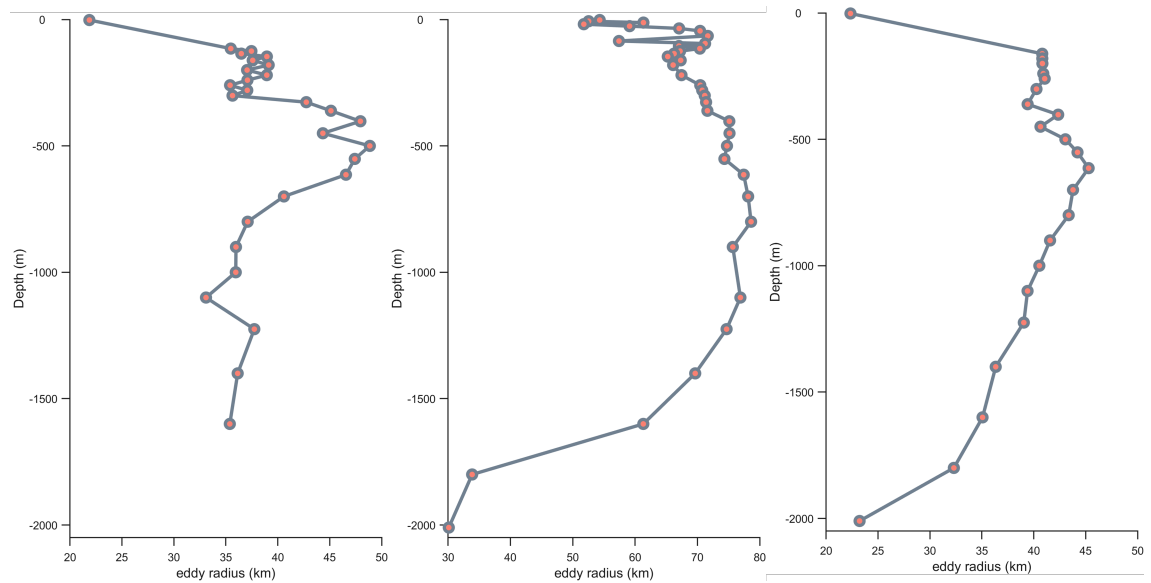


Figure 5.3: Three examples of lens-shaped eddies

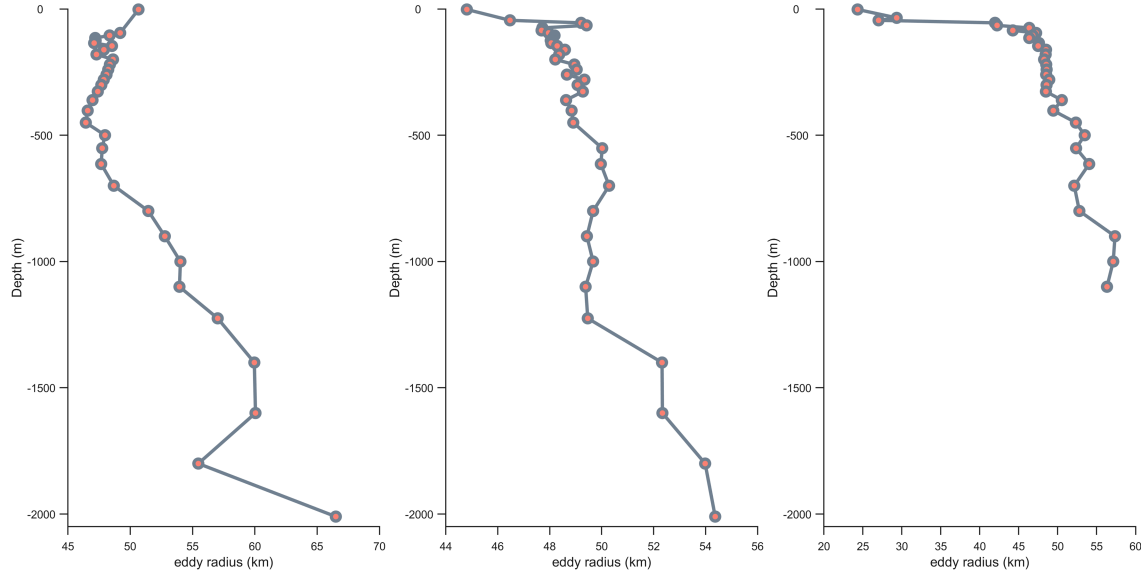


Figure 5.4: Three examples of cone-shaped eddies

salinity is at the blue end of the color chart while the maximum value of the regional salinity is represented by the red color of the color chart; the color bar shown on the left side only displays the salinity limit on the bottom layer. The surface eddy is the center of the negative anomalous envelope of salinity and in the below layers, the eddy is surrounded by high salinity contour. These findings suggest that cold and salty coherent cyclonic eddy may upwell the bottom water column into the subsurface layers.

Figure 5.6 shows an anticyclonic eddy with maximum radius in the intermediate layer and $t_0 = 2014 - 12 - 01$. It has a warm core of the water in the center of the eddy. However, the area of the high-temperature contour is much bigger than the area enclosed by the eddy, which we could infer that coherent water transport capabilities carried by the coherent eddy may be much weaker than what we have expected in an Eulerian instantaneous field.

However, in some of the cases, the extreme value of the background salinity (S) or temperature (θ) field does not match the core of the coherent eddies. In some of the cases, the background

extrema of S or θ may shift a little bit from the eddy center. This asymmetry feature is more obvious in the vertical structure of anticyclonic eddies [65].

What is more, the above rules are not so robust in the surface layer, especially the first 100 meters, which suggests the other boundary layer mixing processes can significantly affect the character of the vortex.

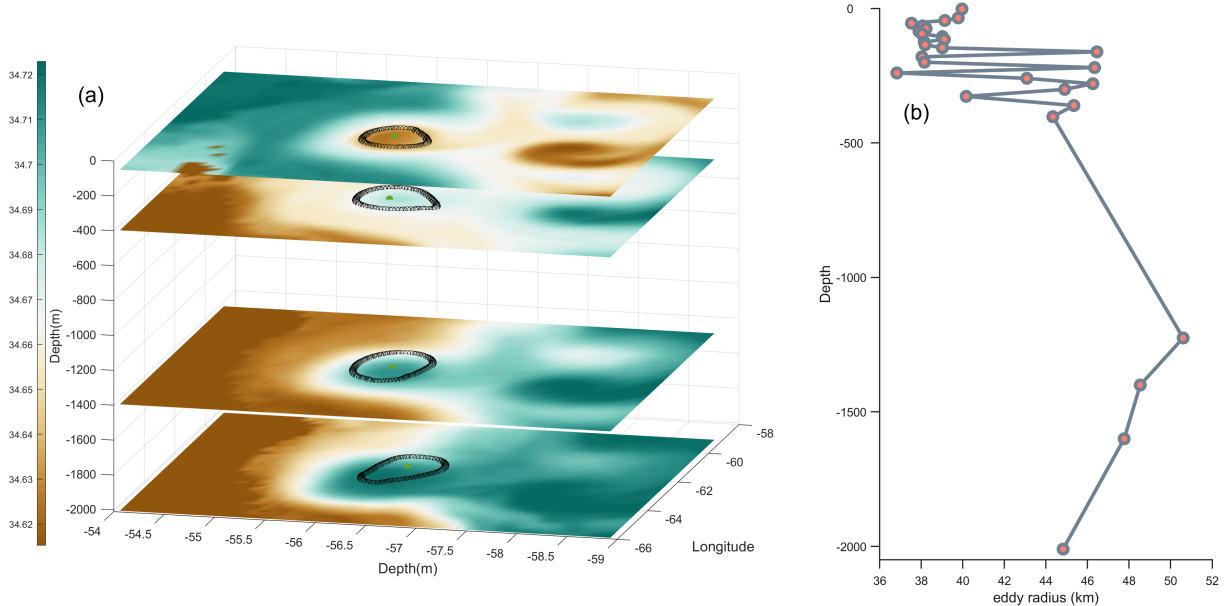


Figure 5.5: Vertical structure of a cyclonic eddy

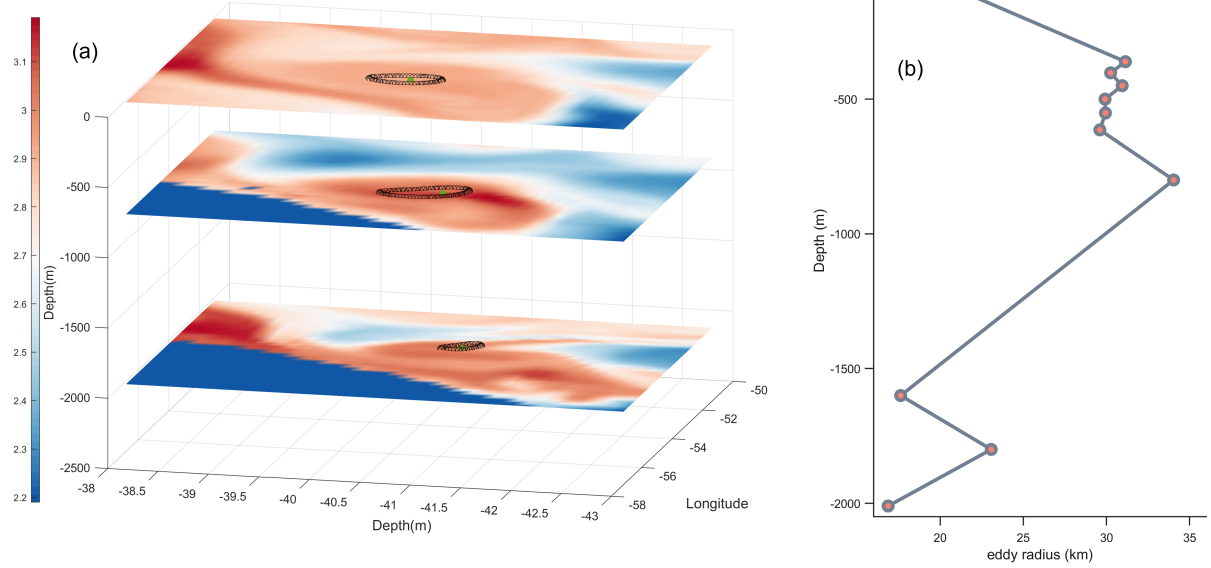


Figure 5.6: Vertical structure of an anticyclonic eddy

5.5 Discussion and Conclusion

Due to the limiting subsurface observational data, we build the three-dimensional structure of coherent eddies using model simulations.

It is still questionable if we do capture the correct shape and penetration depth of coherent eddies and the visualization of propagation of three-dimensional eddies in the real oceanic flow is still on the way [66]. We track surface eddies in this chapter and we attempt to trace the corresponding vortex signal in the subsurface.

We have found three types of eddies in the study period (2013-2018), most of them are lens-shaped eddies having a maximum radius in the intermediate layer. Cyclonic eddies have the tendency to extend in the vertical direction. Eddies could alter the thermohaline properties of seawater: the cyclonic vortex is colder and saltier than the surrounding water column while the anticyclonic eddy is warmer and fresher.

CHAPTER 6

CONCLUSION AND PROSPECT

6.1 Statistics result of coherent eddies in the Argentine Basin

There is an upward trend of eddies in the research domain. Lots of eddies have been observed in the southwest part of the AB and the center part of the AB is the 'Grave' of the Vortex. When we extend the coherence time, the percentage of anticyclonic eddies starts to become larger.

Eulerian eddy's radius is almost twice as large as a Lagrangian coherent eddy.

6.2 Three-dimensional structure of coherent eddies

There are three types of oceanic eddy and lens-shaped eddy is the most common type. Oceanic eddies can strongly affect the thermohaline properties of seawater. Cyclonic eddy is deeper than anticyclonic eddy.

6.3 Future work plan

Although some progress has been made in the work of this paper, there are still many issues that need to be studied and discussed further.

My future research plan mainly focuses on the dynamic mechanism that is related to the formation and temporal and spatial variation of eddies in the study region and how oceanic eddies

modify water mass properties and have a far-reaching impact on the regional and global climate systems. The future work plans are as follows:

- 1) Model data may have large differences in matching with satellite data, and there are limitations in constructing 3D eddies. In the future, we can have a more in-depth understanding of the 3D structure of eddies and the temperature and salt fields from continuous observations of field data such as Argo buoy profiles.
- 2) The relationship between mesoscale eddies and the background flow field, and the characteristics of eddies under different climatic background conditions need further study.
- 3) The transport capacity of vortex-induced heat, energy, and water masses on long-time scales needs to be studied in depth.
- 4) Other relevant and interdisciplinary studies such as interactions and feedback processes between oceanic eddies and the atmosphere, effects of eddies on the marine ecosystem, application of extraction of the skeleton in the geophysical flow field, etc.

REFERENCES

- [1] Dennis J McGillicuddy Jr, Laurence A Anderson, Nicholas R Bates, Thomas Bibby, Ken O Buesseler, Craig A Carlson, Cabell S Davis, Courtney Ewart, Paul G Falkowski, Sarah A Goldthwait, et al. Eddy/wind interactions stimulate extraordinary mid-ocean plankton blooms. *Science*, 316(5827):1021–1026, 2007.
- [2] Zhengguang Zhang, Wei Wang, and Bo Qiu. Oceanic mass transport by mesoscale eddies. *Science*, 345(6194):322–324, 2014.
- [3] James C McWilliams. The vortices of two-dimensional turbulence. *Journal of Fluid mechanics*, 219:361–385, 1990.
- [4] Dudley B Chelton, Michael G Schlax, and Roger M Samelson. Global observations of nonlinear mesoscale eddies. *Progress in oceanography*, 91(2):167–216, 2011.
- [5] Thomas Peacock and George Haller. Lagrangian coherent structures: The hidden skeleton of fluid flows. *Physics today*, 66(2):41, 2013.
- [6] George Haller. Lagrangian coherent structures. *Annual Review of Fluid Mechanics*, 47:137–162, 2015.
- [7] George Haller. A variational theory of hyperbolic lagrangian coherent structures. *Physica D: Nonlinear Phenomena*, 240(7):574–598, 2011.

- [8] Francisco J Beron-Vera, Yan Wang, María J Olascoaga, Gustavo J Goni, and George Haller. Objective detection of oceanic eddies and the agulhas leakage. *Journal of Physical Oceanography*, 43(7):1426–1438, 2013.
- [9] George Haller and Francisco J Beron-Vera. Coherent lagrangian vortices: The black holes of turbulence. *Journal of Fluid Mechanics*, 731, 2013.
- [10] Francesco Nencioli, Changming Dong, Tommy Dickey, Libe Washburn, and James C McWilliams. A vector geometry-based eddy detection algorithm and its application to a high-resolution numerical model product and high-frequency radar surface velocities in the southern california bight. *Journal of atmospheric and oceanic technology*, 27(3):564–579, 2010.
- [11] Francisco J Beron-Vera, María J Olascoaga, Yan Wang, Joaquín Triñanes, and Paula Pérez-Brunius. Enduring lagrangian coherence of a loop current ring assessed using independent observations. *Scientific reports*, 8(1):1–12, 2018.
- [12] Qiu He, Fenglin Tian, Xiaokun Yang, and Ge Chen. Lagrangian eddies in the northwestern pacific ocean. *Journal of Oceanology and Limnology*, 40(1):66–77, 2022.
- [13] Yan Wang, María Josefina Olascoaga, and Francisco J Beron-Vera. Coherent water transport across the south atlantic. *Geophysical Research Letters*, 42(10):4072–4079, 2015.
- [14] Loic Jullion, Karen J Heywood, Alberto C Naveira Garabato, and David P Stevens. Circulation and water mass modification in the brazil–malvinas confluence. *Journal of Physical Oceanography*, 40(5):845–864, 2010.

- [15] Ronald Buss de Souza, Maurício M Mata, Carlos AE Garcia, Milton Kampel, Eduardo N Oliveira, and Joao A Lorenzzetti. Multi-sensor satellite and in situ measurements of a warm core ocean eddy south of the brazil–malvinas confluence region. *Remote Sensing of Environment*, 100(1):52–66, 2006.
- [16] Wilbert Weijer, Alice Barthel, Milena Veneziani, and Hannah Steiner. The zapiola anticyclone: A lagrangian study of its kinematics in an eddy-permitting ocean model. *Deep Sea Research Part I: Oceanographic Research Papers*, 164:103308, 2020.
- [17] Eleanor Frajka-Williams, Isabelle J Ansorge, Johanna Baehr, Harry L Bryden, Maria Paz Chidichimo, Stuart A Cunningham, Gokhan Danabasoglu, Shenfu Dong, Kathleen A Donohue, Shane Elipot, et al. Atlantic meridional overturning circulation: Observed transport and variability. *Frontiers in Marine Science*, page 260, 2019.
- [18] William K Dewar. Topography and barotropic transport control by bottom friction. *Journal of Marine Research*, 56(2):295–328, 1998.
- [19] Lynne D Talley. *Descriptive physical oceanography: an introduction*. Academic press, 2011.
- [20] Marcos Fontela, Antón Velo, Miguel Gilcoto, and Fiz F Pérez. Anthropogenic co₂ and ocean acidification in argentine basin water masses over almost five decades of observations. *Science of The Total Environment*, 779:146570, 2021.
- [21] Dean Roemmich and John Gilson. Eddy transport of heat and thermocline waters in the north pacific: A key to interannual/decadal climate variability? *Journal of Physical Oceanography*, 31(3):675–687, 2001.

- [22] Paulo HR Calil, Kelvin J Richards, Yanli Jia, and Robert R Bidigare. Eddy activity in the lee of the hawaiian islands. *Deep Sea Research Part II: Topical Studies in Oceanography*, 55(10-13):1179–1194, 2008.
- [23] Dudley B Chelton, Michael G Schlax, Roger M Samelson, and Roland A de Szoeke. Global observations of large oceanic eddies. *Geophysical Research Letters*, 34(15), 2007.
- [24] George Haller and Guocheng Yuan. Lagrangian coherent structures and mixing in two-dimensional turbulence. *Physica D: Nonlinear Phenomena*, 147(3-4):352–370, 2000.
- [25] Hassan Aref, John R Blake, Marko Budišić, Silvana SS Cardoso, Julyan HE Cartwright, Herman JH Clercx, Kamal El Omari, Ulrike Feudel, Ramin Golestanian, Emmanuelle Gouillart, et al. Frontiers of chaotic advection. *Reviews of Modern Physics*, 89(2):025007, 2017.
- [26] Joao H Bettencourt, Cristóbal López, and Emilio Hernández-García. Oceanic three-dimensional lagrangian coherent structures: A study of a mesoscale eddy in the benguela upwelling region. *Ocean Modelling*, 51:73–83, 2012.
- [27] James F Price. *Lagrangian and eulerian representations of fluid flow: Kinematics and the equations of motion*. MIT OpenCourseWare, 2006.
- [28] Shawn C Shadden, Francois Lekien, and Jerrold E Marsden. Definition and properties of lagrangian coherent structures from finite-time lyapunov exponents in two-dimensional aperiodic flows. *Physica D: Nonlinear Phenomena*, 212(3-4):271–304, 2005.
- [29] George Haller and Themistoklis Sapsis. Lagrangian coherent structures and the smallest finite-time lyapunov exponent. *Chaos: An Interdisciplinary Journal of Nonlinear Science*,

21(2):023115, 2011.

- [30] E Aurell, Guido Boffetta, A Crisanti, G Paladin, and A Vulpiani. Predictability in the large: an extension of the concept of lyapunov exponent. *Journal of Physics A: Mathematical and General*, 30(1):1, 1997.
- [31] Binson Joseph and Bernard Legras. Relation between kinematic boundaries, stirring, and barriers for the antarctic polar vortex. *Journal of the Atmospheric Sciences*, 59(7):1198–1212, 2002.
- [32] Francesco d’Ovidio, Vicente Fernández, Emilio Hernández-García, and Cristóbal López. Mixing structures in the mediterranean sea from finite-size lyapunov exponents. *Geophysical Research Letters*, 31(17), 2004.
- [33] George Haller. Distinguished material surfaces and coherent structures in three-dimensional fluid flows. *Physica D: Nonlinear Phenomena*, 149(4):248–277, 2001.
- [34] Daniel Karrasch and George Haller. Do finite-size lyapunov exponents detect coherent structures? *Chaos: An Interdisciplinary Journal of Nonlinear Science*, 23(4):043126, 2013.
- [35] Ling Feng, Chuanyu Liu, Armin Köhl, Detlef Stammer, and Fan Wang. Four types of baroclinic instability waves in the global oceans and the implications for the vertical structure of mesoscale eddies. *Journal of Geophysical Research: Oceans*, 126(3):e2020JC016966, 2021.
- [36] Vicky Verma and Sutanu Sarkar. Lagrangian three-dimensional transport and dispersion by submesoscale currents at an upper-ocean front. *Ocean Modelling*, 165:101844, 2021.

- [37] Daniel Mukiibi, Gualtiero Badin, and Nuno Serra. Three-dimensional chaotic advection by mixed layer baroclinic instabilities. *Journal of Physical Oceanography*, 46(5):1509–1529, 2016.
- [38] Kaylie Cohanim, Ken X Zhao, and Andrew L Stewart. Dynamics of eddies generated by sea ice leads. *Journal of Physical Oceanography*, 51(10):3071–3092, 2021.
- [39] Chi Xu, Xiaoming Zhai, and Xiao-Dong Shang. Work done by atmospheric winds on mesoscale ocean eddies. *Geophysical Research Letters*, 43(23):12–174, 2016.
- [40] Lionel Renault, Patrick Marchesiello, Sébastien Masson, and James C Mcwilliams. Remarkable control of western boundary currents by eddy killing, a mechanical air-sea coupling process. *Geophysical Research Letters*, 46(5):2743–2751, 2019.
- [41] Fangyuan Teng, Changming Dong, Jinlin Ji, Brandon J Bethel, Aijun Pan, and Chi Xu. Does the wind stress always damp an oceanic eddy? *Geoscience Letters*, 8(1):1–6, 2021.
- [42] N Ducet, Pierre-Yves Le Traon, and Gilles Reverdin. Global high-resolution mapping of ocean circulation from topex/poseidon and ers-1 and-2. *Journal of Geophysical Research: Oceans*, 105(C8):19477–19498, 2000.
- [43] Guangjun Xu, Cheng Cheng, Wenxian Yang, Wenhong Xie, Lingmei Kong, Renlong Hang, Furong Ma, Changming Dong, and Jingsong Yang. Oceanic eddy identification using an ai scheme. *Remote Sensing*, 11(11):1349, 2019.
- [44] R Laxenaire, S Speich, Bruno Blanke, Alexis Chaigneau, C Pegliasco, and A Stegner. Anticyclonic eddies connecting the western boundaries of indian and atlantic oceans. *Journal of Geophysical Research: Oceans*, 123(11):7651–7677, 2018.

- [45] Matthew R Mazloff, Patrick Heimbach, and Carl Wunsch. An eddy-permitting southern ocean state estimate. *Journal of Physical Oceanography*, 40(5):880–899, 2010.
- [46] Ariane Verdy and Matthew R Mazloff. A data assimilating model for estimating southern ocean biogeochemistry. *Journal of Geophysical Research: Oceans*, 122(9):6968–6988, 2017.
- [47] Changming Dong, Xiayan Lin, Yu Liu, Francesco Nencioli, Yi Chao, Yuping Guan, Dake Chen, Tommy Dickey, and James C McWilliams. Three-dimensional oceanic eddy analysis in the southern California bight from a numerical product. *Journal of Geophysical Research: Oceans*, 117(C7), 2012.
- [48] Wilbert Weijer, Mathew E Maltrud, William B Homoky, Kurt L Polzin, and Leo RM Maas. Eddy-driven sediment transport in the Argentine basin: Is the height of the zapiola rise hydrodynamically controlled? *Journal of Geophysical Research: Oceans*, 120(3):2096–2111, 2015.
- [49] Peter M Saunders and Brian A King. Bottom currents derived from a shipborne adcp on woce cruise a11 in the south atlantic. *Journal of Physical Oceanography*, 25(3):329–347, 1995.
- [50] Jens Kasten, Ingrid Hotz, Bernd R Noack, and Hans-Christian Hege. On the extraction of long-living features in unsteady fluid flows. In *Topological Methods in Data Analysis and Visualization*, pages 115–126. Springer, 2011.
- [51] George Haller and Francisco J Beron-Vera. Geodesic theory of transport barriers in two-dimensional flows. *Physica D: Nonlinear Phenomena*, 241(20):1680–1702, 2012.

- [52] Yan Wang. *Identification and tracking of coherent Agulhas current rings*. University of Miami, 2015.
- [53] George Haller. Lagrangian coherent structures from approximate velocity data. *Physics of fluids*, 14(6):1851–1861, 2002.
- [54] Daniel Blazevski and George Haller. Hyperbolic and elliptic transport barriers in three-dimensional unsteady flows. *Physica D: Nonlinear Phenomena*, 273:46–62, 2014.
- [55] Yan Wang, Francisco J Beron-Vera, and María Josefina Olascoaga. The life cycle of a coherent lagrangian agulhas ring. *Journal of Geophysical Research: Oceans*, 121(6):3944–3954, 2016.
- [56] Clifford Truesdell and Walter Noll. The non-linear field theories of mechanics. In *The non-linear field theories of mechanics*, pages 1–579. Springer, 2004.
- [57] George Haller, Alireza Hadjighasem, Mohammad Farazmand, and Florian Huhn. Defining coherent vortices objectively from the vorticity. *Journal of Fluid Mechanics*, 795:136–173, 2016.
- [58] Nathaniel Tarshish, Ryan Abernathey, Ci Zhang, Carolina O Dufour, Ivy Frenger, and Stephen M Griffies. Identifying lagrangian coherent vortices in a mesoscale ocean model. *Ocean Modelling*, 130:15–28, 2018.
- [59] Qiong Xia, Gaocong Li, and Changming Dong. Global oceanic mass transport by coherent eddies. *Journal of Physical Oceanography*, 2022.
- [60] Rahel Vortmeyer-Kley, Ulf Gräwe, and Ulrike Feudel. Detecting and tracking eddies in

oceanic flow fields: a lagrangian descriptor based on the modulus of vorticity. *Nonlinear Processes in Geophysics*, 23(4):159–173, 2016.

- [61] Daniel McCoy, Daniele Bianchi, and Andrew L Stewart. Global observations of submesoscale coherent vortices in the ocean. *Progress in Oceanography*, 189:102452, 2020.
- [62] Fernando Andrade-Canto, D Karrasch, and Francisco J Beron-Vera. Genesis, evolution, and apocalypse of loop current rings. *Physics of Fluids*, 32(11):116603, 2020.
- [63] Alexis Chaigneau, Marie Le Texier, Gérard Eldin, Carmen Grados, and Oscar Pizarro. Vertical structure of mesoscale eddies in the eastern south pacific ocean: A composite analysis from altimetry and argo profiling floats. *Journal of Geophysical Research: Oceans*, 116(C11), 2011.
- [64] Xiayan Lin, Changming Dong, Dake Chen, Yu Liu, Jingsong Yang, Bin Zou, and Yuping Guan. Three-dimensional properties of mesoscale eddies in the south china sea based on eddy-resolving model output. *Deep Sea Research Part I: Oceanographic Research Papers*, 99:46–64, 2015.
- [65] NV Sandalyuk and TV Belonenko. Three-dimensional structure of the mesoscale eddies in the agulhas current region from hydrological and altimetry data. *Russian Journal of Earth Sciences*, 21(4):5, 2021.
- [66] Yi Liu, Chris Wilson, Melissa A Green, and Chris W Hughes. Gulf stream transport and mixing processes via coherent structure dynamics. *Journal of Geophysical Research: Oceans*, 123(4):3014–3037, 2018.